ABSTRACT

Title of Document: **Atomic Layer Deposition of Ru and RuO_2: New Process Development, Fabrication of Heterostructured Nanoelectrodes, and Applications in Energy Storage**

Keith E. Gregorczyk, Doctor of Philosophy, 2013

Directed By: Professor Gary W. Rubloff, Minta Martin Professor of Engineering, Department of Materials Science & Engineering and Institute for Systems Research

The ability to fabricate heterostructured nanomaterials with each layer of the structure having some specific function, i.e. energy storage, charge collection, etc., has recently attracted great interest. Of the techniques capable of this type of process, atomic layer deposition (ALD) remains unique due to its monolayer thickness control, extreme conformality, and wide variety of available materials. This work aims at using ALD to fabricate fully integrated heterostructured nanomaterials.

To that end, two ALD processes, using a new and novel precursor, bis(2,6,6-trimethyl-cyclohexadienyl)ruthenium, were developed for Ru and RuO_2 showing stable growth rates of 0.5 Å/cycle and 0.4 Å/cycle respectively. Both process are discussed and compared to similar processes reported in the literature. The Ru process is shown to have significantly lower nucleation while the RuO_2 is the first fully characterized ALD process known.

Using the fully developed RuO_2 ALD process, thin film batteries were fabricated and tested in standard coin cell configurations. These cells showed high first cycle gravimetric capacities of ~1400 mAh/g, which significantly degraded after ~40 cycles. Rate performance was also studied and showed a decrease in 1st cycle capacity as a function of increased rate. These results represent the first reports of any RuO_2 battery studied beyond 3 cycles.

To understand the degradation mechanisms witnessed in the thin film studies in-situ TEM experiments were conducted. Single crystal RuO_2 nanowires were grown using a vapor transport method. These nanowires were cycled inside a TEM using Li_2O as an electrolyte and showed a ~95% volume expansion after lithiation, ~26% of which was irreversible. Furthermore, a chemical irreversibility was also witnessed, where the reaction products Ru and Li_2O remain even after full delithiation.

With these mechanisms in mind heterostructured nanowires were fabricated in an attempt to improve the cycling performance. Core/shell TiN/RuO_2 and MWCNT/RuO_2 structures were fabricating using the ALD process developed in this work. While the TiN/RuO_2 structures did not show improved cycling performance due to connection issues, the MWCNT/RuO_2 structure showed a stable areal capacity of ~600 μAh/cm^2 after ~20 cycles and were easily cycled 100 times.

ATOMIC LAYER DEPOSITION OF RU AND RUO_2: NEW PROCESS DEVELOPMENT, FABRICATION OF HETEROSTRUCTURED NANOELECTRODES, AND APPLICATIONS IN ENERGY STORAGE

By

Keith E. Gregorczyk

Dissertation submitted to the Faculty of the Graduate School of the
University of Maryland, College Park, in partial fulfillment
of the requirements for the degree of
Doctor of Philosophy
2013

Advisory Committee:
Professor Gary Rubloff, Chair
Professor Sang Bok Lee
Professor Raymond Adomaitis
Professor Eric Wachsman
Professor Liangbing Hu

Dedication

To my family

Acknowledgements

This work would not have been possible were it not for a very large number of people. To my fellow classmates; Gary, Mark, Paris, Krista, Adam, and Zane, thanks for always knowing where the gold at, what the whistle do (it go whooo!), finding bread on trains, grad pubs, and sometimes doing homework. To Amy for long runs and deep conversations, bike rides and picnics, cooking and KAFKC, books and all of our other random adventures, thanks. To my group mates, Parag, Laurent, Xinyi, Alex, Marshall, Yi, and Xialong thanks for being wealth of knowledge and assistance.

To my advisor Gary Rubloff, thank you for hiring me after I had already wasted a year working for someone else and trusting me enough to follow several crazy ideas, most of which failed miserably, but taught me a lot.

To Kathleen Hart for helping me navigate the paper work of grad school and getting me through one of the worst crisis of my life. I am forever indebted to you. To the support staff at University of Maryland no amount of thank you’s is enough but thank you!

Finally and most importantly this work is dedicated to my family. To my Grandfather Stephen for making me ‘do my letters and numbers’ every Sunday morning, inadvertently (or more likely advertently) instilling me with an absolute love of knowledge, thank you. To my Grandfather Harvey for showing me what true bravery and courage is, apologizing when you know you were wrong. To my Grandmothers Helen and Mary for showing what unconditional love looks like, if they are angels, or things made of them, it would certainly be you two, I wish I could have known you better.

To my little brother, my friend, if you learn anything from me let it be that anything is possible with, blood, sweat, tears, and a little blind ambition.

To my Mother and Father for their support, trust, and love. To being a foundation for me to stand on and reach heights not fathomable for a poor kid from New Britain. It has been a long, often hard, but ultimately joyous road and I couldn't have done it without you. You are all that I am and I love you both dearly.

Finally, this work has been partially supported by Nanostructures for Electrical Energy Storage (NEES), an Energy Frontier Research Center funded by the U.S. Department of Energy, Office of Science, Office of Basic Energy Sciences under Award Number DESC0001160 and partially supported by the L-3 Communications fellowship.

Table of Contents

Chapter 1: Introduction and Motivation

1.1 Motivation

To meet the growing demand for energy world wide, renewable sources are predicted to play a larger role and may significantly replace fossil fuels. There are a number of renewable sources available such as; solar, wind, geothermal, hydroelectric, etc. However, each of these has problems concerning delivery and storage. Wind and solar peak energy production does not always overlap with peak demand, and geothermal and hydroelectric sources are often remote relative to areas of high demand. One way to combat these two problems simultaneously is to store the energy, either as a charge (as is done in capacitors) or electrochemically (as is done with ions in a battery), so it can be used when and where it is most needed. To achieve this, significant advances are required in both energy density, i.e. the amount of energy that can be stored per unit mass or volume, and power density, i.e., the rate at which energy can be delivered per unit mass or volume.

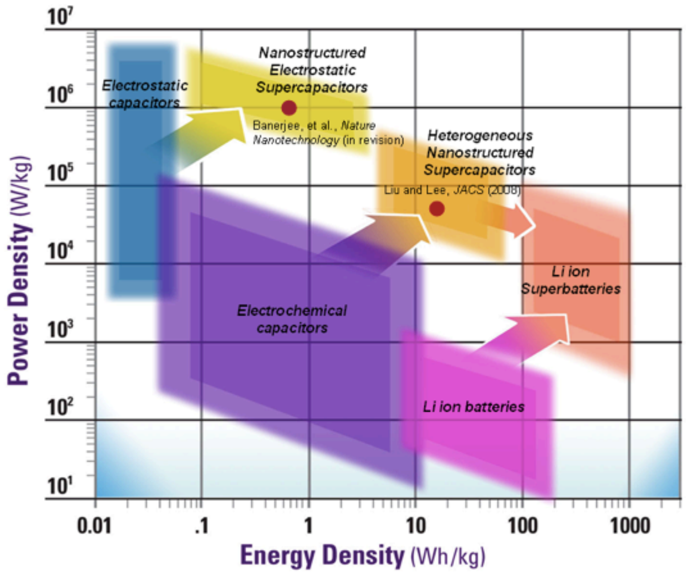

Figure 1. Ragone plot for electrochemical energy storage devices. Showing the energy and power density for traditional capacitors and batteries, and the dramatic improvements possible by using heterostructured nanomaterials.

Techniques to precisely control the shape and structure of nano-sized materials have been maturing over the past twenty years, allowing one to grow structures of a precise thickness, size, and shape [2]. These same techniques have been adapted to make more complicated heterostructure nanomaterials and have recently been able to show significant improvement in energy storage. This can be seen in Figure 1, which shows a Ragone plot of different electrical energy storage devices (EESD). This plot is important for a number of reasons; first it shows the fundamental limitations of traditional EESD's. Due to differences in storage mechanisms of capacitors, which store energy as surface charge, and batteries, which store ionized species, we typically see a trade off between high power density and high energy density. Secondly, we see that by using heterostructured nanomaterials, significant improvements can be made, as was shown by Banerjee *et al* for electrostatic capacitors [3] and Liu and Lee for electrochemical capacitors [4].

Both of these results took advantage of highly ordered, nano-porous anodized aluminum oxide (AAO) templates [5]. These templates are grown electrochemically and can have pore diameters ranging from 40-200nm with pore lengths from 100nm to 50µm, allowing the growth of structures with incredibly high aspect ratios (depth/width = 200). Pore densities can be on the order of $\sim 10^{10}$ pores/cm^2 which is equivalent to a 100x increase in surface area for an aspect ratio of 200. Two separate deposition techniques were used; Liu and Lee used electrodeposition while Banerjee *et al* used atomic layer deposition (ALD).

1.2 A Brief Introduction to Atomic Layer Deposition

ALD is a gas phase deposition technique that uses sequentially pulsed, self-limiting reactions between metal-organic and oxidant (typically H_2O or O_2) precursors to grow oxide, sulfide, phosphide, metal, and a variety of other materials one monolayer at a time [6]. This self-limiting behavior allows unprecedented uniformity, conformality, monolayer thickness control, and a wide variety of available materials including, but certainly not limited to; Al_2O_3, TiO_2, TiN, ZnO, V_2O_5, Ru, and RuO_2. A larger list, which includes some 75 elements and 125 compounds, can be found in the following reference [7]. A more detailed review of this technique is presented in chapter 2.1.

1.3 ALD in Electrochemical Energy Storage

Recently ALD has been used to significantly improve the performance of a number of standard cathode and anode materials in Li-ion batteries (LIBs) by using ultrathin passive coatings (i.e. materials that themselves have negligible Li^+ storage capacities). For cathodes, ultrathin coatings of Al_2O_3, TiO_2, and ZnO on composite $LiCoO_2$/C, composite $LiCoO_2$/poly(vinylidene)fluoride, and nanoparticle $LiCoO_2$ powders, showed increased cycling stability and durability, and high power and energy densities [8-12]. Similar results have been reported for ZnO coated $LiMn_2O_4$ and Al_2O_3 coated $Li[Li_{0.2}Mn_{0.54}Ni_{0.13}Co_{0.13}]O_2$ [13, 14]. Ultrathin Al_2O_3 coatings were also shown to reduce capacity fade during cycling, increase columbic efficiency, and increase mechanical integrity of high volume expansion anode materials such as MoO_3 and α-Si[15-17]. Increased stability and capacity was also seen for Al_2O_3-coated carbon nanotubes [18].

A few reports exploiting ALD's extreme conformality have shown dramatic increases in areal capacity when active materials are deposited on, or into, high surface area substrates, such as nanowires, nanorods, and/or nanopores. For anodes, the relatively low capacity material TiO_2 (150 mAh/g) has been deposited on Al nanorods, Ni nanowires, and bio-templated tobacco mosaic virus (TMV) substrates [19-22]. ALD processes have also been developed for higher capacity materials such as Co_3O_4 (374 mAh/g) for cathodes and SnO_2 (782 mAh/g) for anodes [23, 24]. Recently our group has developed a new process capable of depositing crystalline V_2O_5, a cathode material with a relatively high theoretical capacity (294 mAh/g, forming $Li_2V_2O_5$) [25] and applied it to make high surface area electrodes using TMV and multiwall carbon nanotube (MWCNT) sponges [26-28]. With these promising results, the available selection of electrochemically active materials through ALD continues to expand toward higher capacity materials.

1.4 Why RuO_2

Ruthenium is reported to have six possible oxidation states, most of which only exist under extreme conditions [29]. RuO may exist as a gas under some unspecified conditions, RuO_3 as a vapor at 1200° C [30], RuO_4 which melts at 25.4°C and boils at 40°C, Ru_2O_3 which has never been isolated but has been observed in a hydrated form, $Ru_2O_3 \bullet H_2O$, and is reported to have a corundum structure[31], and Ru_2O_5 which has little mention in the literature. This leaves RuO_2, a highly stable, semi-transparent, deep blue material which exhibits metallic conductivity due to the Fermi level lying in the conduction band which has been shown to be comprised of mostly Ru-4d orbitals [32]. RuO_2 has a low bulk resistivity of 36 $\mu\Omega$ cm when in single crystal form, which is a rutile structure with lattice parameters a=4.492 Å and c=3.107 Å [33]. When compared to other conductors it exhibits higher electrical conductivity than roughly one-third of all pure metals [34].

RuO_2 has been used for a variety of applications including catalysis of chlorine and oxygen, photochemical water decomposition, and most importantly for this work, as a high capacity energy storage material [35-37]. Most notable, however, is its application in electrochemical supercapacitors where it shows a high specific capacity with a range of reported values (~200-1200 Fg^{-1}) shown to be highly dependent on the amount of water in the material [38]. Significantly less reported has been its application as a battery material, where it was shown to have a high specific capacity of 1130 mAh/g [39, 40]. The first use of RuO_2 was reported by Trasatti and Buzzanca in 1971 where it was shown to have a rectangular shaped cyclic voltammogram [41]. Since then a large body of work has been published showing various deposition techniques, geometries, mixtures with other materials, and their respective energy storage capacity.

Though mentioned profusely in battery communities as an ideal battery material very little work has been published concerning RuO_2's performance as a battery material. When a non-aqueous Li based electrolyte, such as the standard $LiPF_6$ in 1:1 EC/DMC, is used RuO_2 behaves like a battery. As a battery electrode RuO_2 shows a high gravimetric capacitance of 1130 mAh/g, which corresponds to 5.6 moles of Li per mole of RuO_2 [39, 40]. It has also been studied as an interconnect for low conductivity $LiFePO_4$ [42], to fabricate nanoporous templates at deep discharge [43], and as a metastable compound capable of higher cell potential [44].

With this in mind it is important to note that Ru is well known in the ALD community as a potential electrode material (reviewed in further detail in Chapter 2.3) and many of the processes for ALD Ru note the possibility of growing RuO_2 (reviewed in further detail in Chaper 2.4) but only for the purpose of preventing it and thus making the most conductive Ru possible. With ALD's emergence as an interesting technique for energy storage systems combined with the interest in RuO_2 in the battery community and since no work exists in the literature showing a fully developed ALD process or using ALD RuO_2 as an energy storage material, a unique and interesting project presented itself.

1.5 Outline of Work

This dissertation is presented in the following order. In Chapter 2, through a calibration with Air Liquide, a newly developed Ru ALD precursor was used to show two ALD processes, for Ru and RuO_2 respectively. Each material is characterized with the results shown in the same chapter.

Chapter 3 uses the fully developed RuO_2 ALD process to fabricate and test thin film batteries. During the study of these batteries it was discovered that there was a significant information gap in the literature concerning the mechanism by which Li^+ is stored in RuO_2. A collaboration between University of Maryland (UMD) and Sandia National Labs (SNL) to use in-situ TEM techniques to study the lithiation techniques was started. The results of these studies are discussed in Chapter 4.

Using the combined knowledge from Chapters 2, 3, and 4 3D TiN/RuO_2 and MWCNT/RuO_2 core shell nanowire arrays were fabricated. The results from this study are discussed in Chapter 5.

Finally the dissertation is concluded in Chapter 6, discussing the significance of the work and future implications.

Chapter 2: Development of Ru and RuO_2 ALD Processes

2.1 What is ALD?

As mentioned in Chapter 1.2, ALD is a gas phase deposition technique with monolayer thickness control and is capable of extreme conformality. This technique was originally developed under the name atomic layer epitaxy (ALE) and was referred to as such until approximately 2000 [45]. The history of technique can be traced back to its development in the 1970s by Suntola *et al* in Finland with the first system being built to deposit ZnS [46]. The original application of the technique was to produce electroluminescent displays with the first commercial device being operated at the Helsinki airport from 1983 to 1998.

Figure 2(a-e) shows a generic schematic of an idealized ALD process. The process starts (a) with a substrate with known surface groups, in this case –OH groups. Next (b) a metal-organic precursor is pulsed into the reaction chamber where it chemisorbs and reacts with the surface species producing by products that are then pumped away (c). The second precursor (d), in this case water, is then exposed to the substrate and reacts with the metal-organic precursor at the surface, again producing by-products that are again pumped away (e). Ideally after one complete cycle a single monolayer of the desired material, in this case some metal oxide, would have been deposited and the surface species will be the same as they were at the start, in this case the –OH species seen in Figure 2 (a) and (e).

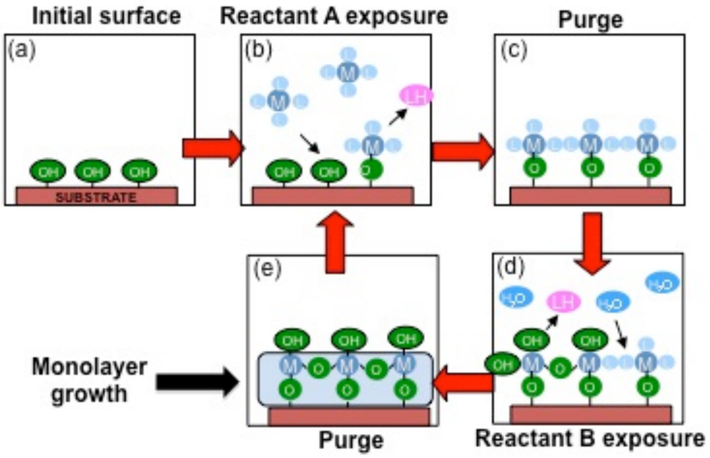

Figure 2. Schematic of an ALD process for a generic ALD process. A process starts (a) with a clean substrate with a hydroxylated surface. Next (b) a metal-organic precursor is pulsed into the reaction chamber and reacts with the –OH surface producing reactants that are pumped away (c). Water is then pulsed into the reactor that reacts with the remaining metal-organic precursor and, again, the by-products are pumped away (e). Theoretically after one cycle a single monolayer of the desired material has been deposited. By repeating this cycle thicker layers can be added one monolayer at a time.

2.1.1 Experimentally Verifying an ALD Process

Four sets of data are required to confirm the self-limiting nature of a potential ALD process. A schematic of these data are shown in Figure 3(a-d). The temperature window, Figure 3(a), has a variety of possible shapes and depends largely on the temperature stability of the metal-organic precursor being used. The ALD window exists in a temperature range where the growth rate per cycle (GPC) is constant. If the temperature is too low the GPC can appear to be higher if the precursors condense on the substrate or lower if the substrate temperature is not high enough to activate the reaction. On the high-temperature side of the ALD window the GPC can again be higher or lower than the window GPC. Increased GPCs are generally attributed to precursor decomposition where the reaction appears to behave more like a CVD process, scaling linearly with temperature, while lower GPCs are the result of precursor desorption.

Figure 3 (b and c) show the standard saturation curves for each of the two precursors. The dose of each precursor is generally controlled by using timed Swaglock ALD valves which allow a fixed amount of precursor, depending on the individual vapor pressures, into a reaction chamber. By varying the time of each pulse the dose of each precursor is effectively controlled. At some precursor dosage all available reaction sites have been used therefore further increases in dosage will not result in larger GPC.

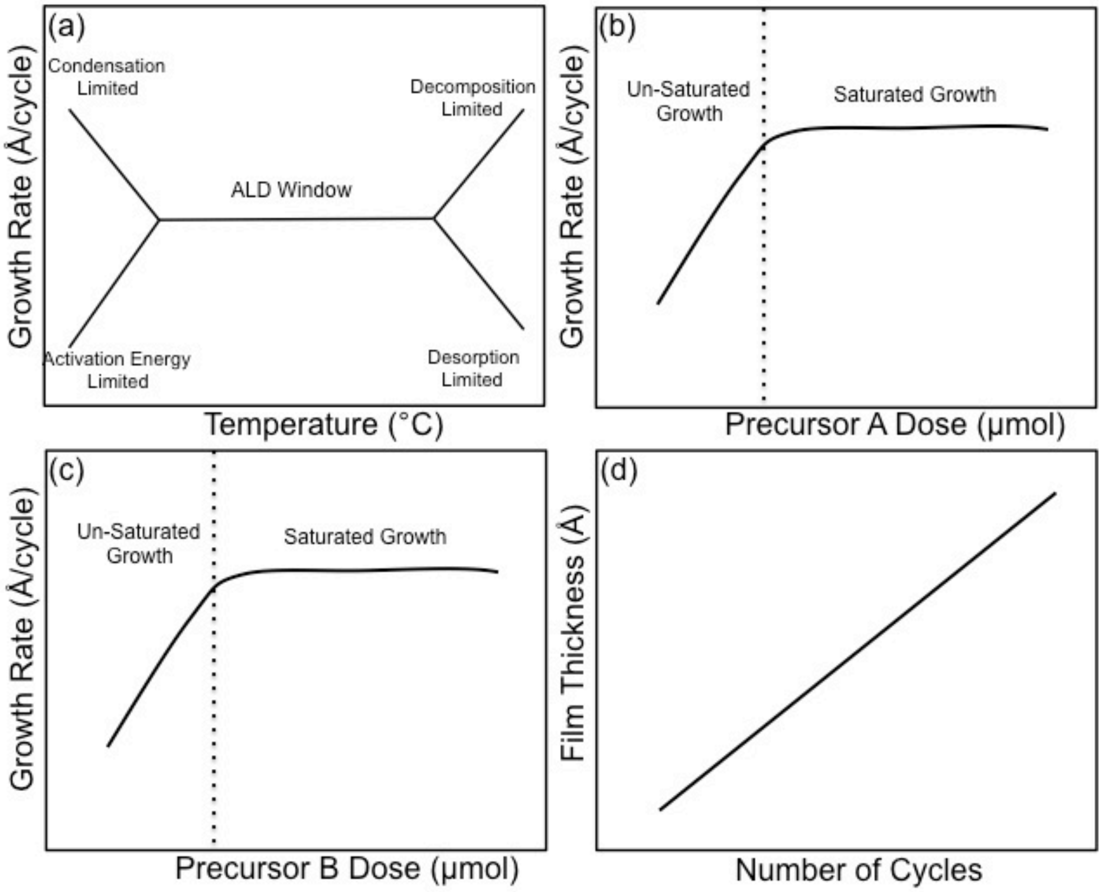

Figure 3. A schematic of an ideal ALD process. (a) shows the possible shape of the temperature data with the ALD window in the middle. The saturation curves for each precursor, denoted A and B, are shown in (b) and (c). The linear growth rate as a function of cycle number is shown in (d).

Figure 3(d) shows the film thickness as a function of cycle number. These data are important for several reasons. First, the slope of the line is the saturated GPC, which should agree the GPC from Figures 3(a-c) and by back-calculating the x-intercept a rough estimate of the number of cycles required for nucleation can be found. The number of cycles can be dependent on a number of variables including, surface species, precursor properties, and type of reaction. Further information about ALD basics can be found in the following reviews [6, 7, 47].

2.1.2 Combustion Type ALD reactions

A variety of 'types' of ALD exist which depend on the how the reaction chemistry proceeds. For standard metal oxide films these types include thermal ALD, which is the most common and includes the standard Al_2O_3-H_2O process, plasma or radical-enhanced ALD, which, as the name implies, uses plasmas or other energetic species (e.g. ozone) to deposit films. Single element and metal films techniques include the previously mentioned plasma-enhanced ALD but also include flourosilane elimination, hydrogen reduction, and most important for this work combustion reactions [45].

Combustion reactions are reactions that produce CO_2 and H_2O when the metal-organic precursor reactions with O_2 and have been used to deposit Ru and Pt films [48, 49]. The Ru and RuO_2 ALD processes in this chapter are discussed in terms of similar reactions using more common Ru based precursors and are generally considered to be combustion reactions.

2.1.3 Experimental Equipment and Procedures

2.1.3.1 Ruthenium ALD

Thermal analysis of $Ru(C_9H_{13})_2$, the results of which are discussed in Chapter 2.3, was conducted in two ways and compared to $Ru(EtCp)_2$. Thermogravimetric measurements were performed using a Mettler-Toledo model STARe TG/SDTA851e system with samples in an inert atmosphere (O_2 and H_2O <5ppm). Both samples were heated at a rate of 10°C/min and these data were used to calculate the vapor pressure of $Ru(C_9H_{13})_2$ and $Ru(EtCp)_2$, while vapor pressure for $RuCp_2$ was taken from the literature [50]. Differential scanning calorimetry (DSC) experiments were performed using a Brucker model DSC3300 system with a heating rate of 10°C/min as well. All samples were prepared under an inert atmosphere (O_2 and H_2O <5ppm). Stability of the $Ru(C_9H_{13})_2$ was observed visually: after exposure to air no color change or temperature change was noticed, which indicated no reaction had occured.

Ruthenium deposition experiments, discussed in Chapter 2.4, were conducted in a wafer-scale cross-flow ALD reactor. This load-locked system houses a 0.2 L reaction chamber operating in the 0.1-1 Torr pressure regime, the relatively small chamber volume being conducive to subsecond residence times. The system features a single-wafer substrate heater, which was calibrated using a SensArray wafer instrumented with 13 thermocouples. Details on the design and operation of this system are discussed in previously published work [51, 52].

Research-grade oxygen (Praxair, 99.999% purity) was delivered through a needle valve and timed Swagelok ALD valve. The Ru precursor was loaded in a Strem electropolished stainless-steel bubbler maintained at 60 °C. Using a three way-valve, 10 sccm N_2 was flowed through the bubbler, the dose being regulated by the actuation time of a downstream ALD valve.

All the experiments were conducted on 4-in (100mm) Si(100) wafers. Si wafers were dipped in a 3% HF solution for 20s, followed by deionized (DI) water rinse and N_2-blow dry prior to being transferred to the load-lock.

To test the ALD growth properties of the $Ru(C_9H_{13})_2$ precursor on different materials, films of SiO_2, TiO_2, and Al_2O_3 were first grown on the wafers. 110 nm SiO_2 films were grown by CVD in a Tystar CVD system. TiO_2 and Al_2O_3 films (25 nm thick) were deposited in a commercial Beneq TFS500 ALD reactor using water as an oxidant and tetrakisdimethylamido titanium (TDMAT) and trimethyl aluminum (TMA), respectively, as metal organic precursors.

Process optimization experiments were conducted exclusively on the SiO_2 coated wafers. Each run consisted of 300 cycles of deposition, unless otherwise noted. Under optimized process conditions, a cycle sequence consisted of a 5s $Ru(C_9H_{13})_2$ pulse, a 15s pump down/purge to return the chamber back to base pressure, a 1s O_2 pulse at 1.2 Torr, and a final 15s pump down.

Film thicknesses were measured ex situ with a Sopra GES5 spectroscopic ellipsometer. Thickness profiles for each wafer, unless otherwise noted, were mapped by measuring a 25-point grid. The average thickness of these points is reported as the thickness and the nonuniformity was estimated from the ratio of the standard deviation of the 25 points divided by the mean. The structure of the films were examined by SEM, using a Hitachi SU-70 Analytical UHR FEG system and Bruker

D8 Discover Powder Diffractometer using Cu Kα radiation and equipped with a Göbel mirror and HiStar area detector to study their morphology and crystallinity.

Electrical measurements were made on samples using Van der Pauw geometry with an Ecopia HMS-5000 Hall effect measurement system in the temperature range of 80-340K. AFM images were acquired using a Digital Instruments model 3100 in tapping mode. RMS roughness and average grain size were calculated using the open source SPM software Gwyddion [53].

2.1.3.2 RuO_2 ALD

Due to a lab fire that occurred on January 16th 2012 the ALD reactor used for the Ru ALD experiments was damaged beyond repair. Therefore all of the RuO_2 ALD experiments, discussed in Chapter 2.4, were don in a different custom reactor. This reactor has a base pressure of 25 mtorr. The metal-organic Ru precursor, bis(2,6,6-trimethyl-cyclohexadienyl)ruthenium, $Ru(C_9H_{13})_2$ (or 'Cyprus', Air Liquide), was loaded into a Strem electropolished stainless-steel bubbler and maintained at 80°C. Ar (99.99%, Praxair) was flowed through the bubbler at 100 sccm. Research grade O_2 (99.999%, Praxair) was used as the oxidant and was flowed at 400 sccm. Timed Swagelok© ALD valves controlled the dose for both precursors. One optimized ALD cycle consisted of the following pulse/purge sequence: 10s $Ru(C_9H_{13})_2$ pulse, 5s Ar purge, 30s O_2 pulse, 5s Ar purge. Process optimization was done on 50mm Si wafers.

Material characterization was done using a Horiba Jobin-Yvon LabRAM HR-VIS MicroRaman system with an internal 632.8 nm laser source. To determine whether the deposited films were crystalline, x-ray diffraction (XRD) was done with a Bruker D8 Advance system with LynxEye PSD detector and Ni β-filter using CuKα radiation. Samples prepared for XRD were deposited on a 1 cm x1 cm glass slide that were cleaned in an acidic piranha solution for 5 min, rinsed with DIW, and blown dry with N_2 before deposition.

AFM images were acquired with a Digital Instruments model 3100 in tapping mode. RMS roughness and average grain size were calculated using the open source SPM software Gwyddion [54]. SEM images were obtained with a Hitachi SU-70.

Film thicknesses were measured ex-situ with a Sopra GES5 spectroscopic ellipsometer. Thickness profiles for each wafer, unless otherwise noted, were mapped by measuring 5 points along the gas flow direction. The average thickness of these points is reported as the thickness and the non-uniformity was estimated from the ratio of the standard deviation of the 5 points divided by the mean.

2.2 A Comparison of Ru based metal organic precursors

The most commonly used Ru ALD precursors belong to the cyclopentadienyl class, which include $RuCp_2$ [25], and $Ru(EtCp)_2$ [21, 26]. Though both have reasonable growth rates per cycle (GPC), i.e., 0.45 Å/cycle and 1.5 Å/cycle respectively, large nucleation barriers on the order of several hundred cycles have been reported, i.e. the GPC is either slow or delayed in reaching a steady state value as a function of ALD cycle number. This limits the ability to accurately control the film thickness, while leading to waste of expensive precursor. The next most common class of Ru precursors, the tris-β-diketonates which includes $Ru(thd)_3$[27, 28], are solid at room temperature (with the exception of $Ru(Od)_3$[29]), and therefore present additional challenges regarding reactant delivery due to their inherently low vapor pressure. Growth rates reported by Aaltonen et al. [27] when using Ru(thd)$_3$ in its solid form were the lowest reported growth rate of all the Ru precursors at 0.36 Å/cycle [27]. Kim et al. dissolved the solid precursor in ethylcyclohexane in order to use a liquid injection system [28]. While self-limiting growth was achieved, the growth per cycle was dependent on both the concentration of Ru(thd)$_3$ solution in ethylcyclohexane and flow rate of the delivery gas through the liquid injection system. Even in this case, the GPC value was not improved with a reported value of ~0.3 Å /cycle reported [28]. A higher GPC, i.e., 0.8 Å /cycle was achieved over a 325-375 °C temperature window in the case of Ru(Od)$_3$ though a liquid injection system was still required, presumably due to its low vapor pressure. Ru(IPMB)(CHD), a custom made precursor, was reported and showed excellent growth rate compared to Cp-based chemistries, high uniformity and conformality, and slow nucleation [30]. The temperature window, however, was not reported and due to the complicated synthesis this precursor does not seem to be readily available. N,N-RuCp was investigated as a high-temperature precursor and showed a saturated growth rate of 0.5 Å /cycle between 400 and 450°C. A table of available Ru-based precursors can be found in Appendix 1.

2.2.1 Other Ruthenium Deposition Techniques

A number of other techniques have been reported for the deposition of Ru. Methods include CVD [55], MOCVD [56], ECD [57, 58], PLD [59], sputtering [60], and electron beam evaporation.

2.3 Precursor Development

In order to address and circumvent issues generated by molecules studied in the literature bis(2,6,6-trimethyl-cyclohexadienyl)ruthenium ($Ru(C_9H_{13})_2$) was developed as a new commercially available ALD precursor [1]. Due to the proprietary nature of its production the exact details of its commercial synthesis cannot be revealed though a more general discussion will help to elucidate its improved performance as an ALD precursor. To understand the properties of this complex, it is informative to discuss the properties of other more common ruthenium complexes. As mentioned in the introduction there are a number of different Ru complexes available which will deposit by ALD. The most commonly used, $Ru(EtCp)_2$, was shown to react with O_2 to deposit Ru [61] but it exhibits very large nucleation delays, on the order of several hundred cycles, that limit the potential for industrialization as was shown in a MOCVD process [62]. In comparison (2,4, dimethylpentadienyl)(ethylcyclopentadienyl)ruthenium, called DER, has also been evaluated in prior work. The difference between these two molecules only originates in the substitutions of one ethylcyclo-pentadienyl ligand by one 2,4,dimethyl-pentadienyl (DMPD) ligand. As a result, it was reported that depositions with shorter nucleation delay were possible using DER [62, 63]. Unfortunately by changing this ligand the same authors [63] noted a marked decrease in the thermal stability, by about 100°C, as compared to $Ru(EtCp)_2$. This decrease in thermal stability of DER was reported to be due to the less stable bonding between the DMPD ligands and the Ru ions [63]. We may conclude that despite the decrease in the thermal stability, it is desirable to replace cyclopentadienyl ligands with more reactive pentadienyl ligands [1].

Our experience shows that (2,4-dimethyl-pentadienyl)(ethylcyclopentadienyl)ruthenium and the related bis(2,4-dimethyl-pentadienyl)ruthenium can only be prepared with low yield from the precursor synthesis process. As a consequence, we considered alternatives to 2,4-dimethylpentadienyl in order to take advantage of the higher reactivity of the outer vinyl carbons. Among them, the cyclohexadienyl structure appears similar to the 2,4-dimethylpentadienyl structure except for the out-of-plane carbon bridging the outer sp^2 carbons, which can be seen in the inset of Figure 4. The edge-bridged open ruthenocene structure of the cyclohexadienyl ligand and the increased steric bulk make this complex more thermally stable than DER or $Ru(EtCp)_2$, and the closed carbon ring was expected to enhance the reactivity of the molecule with the co-reactant O_2. To confirm this, thermogravimetric and DSC measurements were made. Thermogravimetric results for $Ru(C_9H_{13})_2$ is compared to those for $Ru(EtCp)_2$ in Figure 4(a) showing that both molecules evaporate smoothly without leaving significant residue. The temperature of end-of-evaporation is very close for both molecules, implying that the molecules have very similar vapor pressures. The absence of residual mass amounts confirms the thermal stability of both molecules up to 250°C.

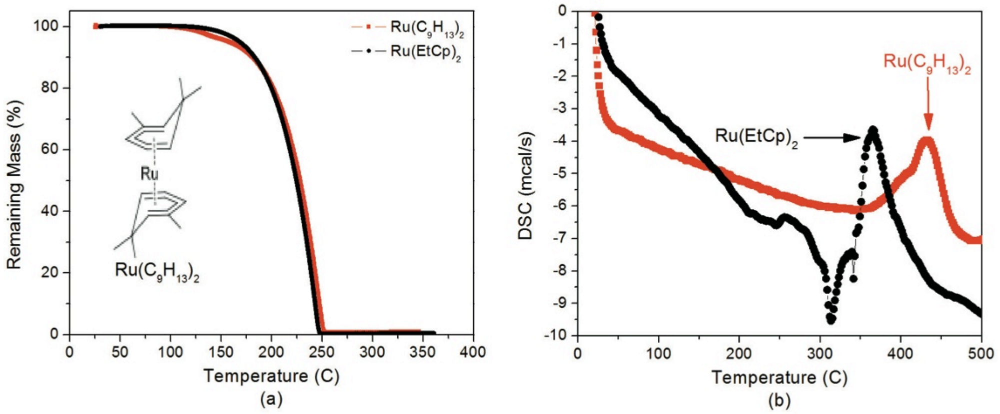

(a)

(b)

Figure 4. Thermal characterization. (a) Thermogravimetric analysis showing a comparison between $Ru(C_9H_{13})_2$ and commonly used $Ru(EtCp)_2$ (inset shows the chemical structure of $Ru(C_9H_{13})_2$ [1]); these data show a smooth evaporation with no signs of decomposition below 250^{o}C. (b) DSC measurements showing thermal breakdown of $Ru(C_9H_{13})_2$, as compared to $Ru(EtCp)_2$; peaks clearly corresponding to an exothermic reaction are seen at 375^{o}C for $Ru(EtCp)_2$ and 425^{o}C for $Ru(C_9H_{13})_2$, confirming the increase in stability.

To investigate the behavior of both molecules at higher temperatures, DSC measurements were made as shown in Figure 4(b). The decomposition onset, which corresponds to an exothermic reaction, is clearly seen at 375°C for $Ru(EtCp)_2$, while an onset at 425°C occurs for $Ru(C_9H_{13})_2$, making it more thermally stable and more reactive with the co-reactant O_2 than both $Ru(EtCp)_2$ and DER. Furthermore the new precursor $Ru(C_9H_{13})_2$, bis(2,6,6-trimethyl-cyclohexadienyl)ruthenium, is a liquid at room temperature, is stable in air, and has a similar vapor pressure to $Ru(EtCp)_2$ and $RuCp_2$, shown in Figure 5, thus making it a suitable candidate for ALD deposition of high quality Ru films.

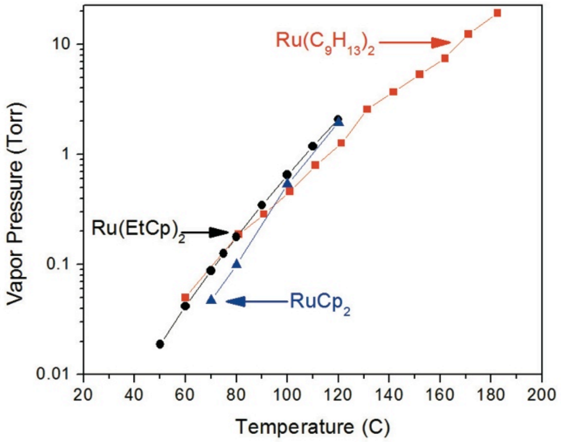

Figure 5. Vapor pressure of $Ru(C_9H_{13})_2$ as compared to Cp complexes, showing a good comparison to commonly used ruthenium precursors.

2.4 Ru ALD

2.4.1 ALD Process Development

To characterize the ability of $Ru(C_9H_{13})_2$ to induce self-limited chemisorbed reactions to achieve ALD's benefits, the metal-organic precursor was used with O_2 in an ALD process carried out in the cross-flow reactor. In Figure 6 the surface saturation of $Ru(C_9H_{13})_2$ and O_2 precursors was investigated by measuring the GPC as a function of $Ru(C_9H_{13})_2$ pulse time (Figure 6a) and O_2 pulse pressure (Figure 6b). The top axis on both figures provides estimations of the corresponding doses in µmol as calculated using a standard bubbler delivery model [64] in the case of $Ru(C_9H_{13})_2$ and an experimental calibration procedure derived from the ideal gas law for the oxygen precursor. In the case of $Ru(C_9H_{13})_2$, pulse time, the growth per cycle (GPC) reaches a plateau at 0.5 Å/cycle for exposure above 3s (2.2 µmol) as Ru-based

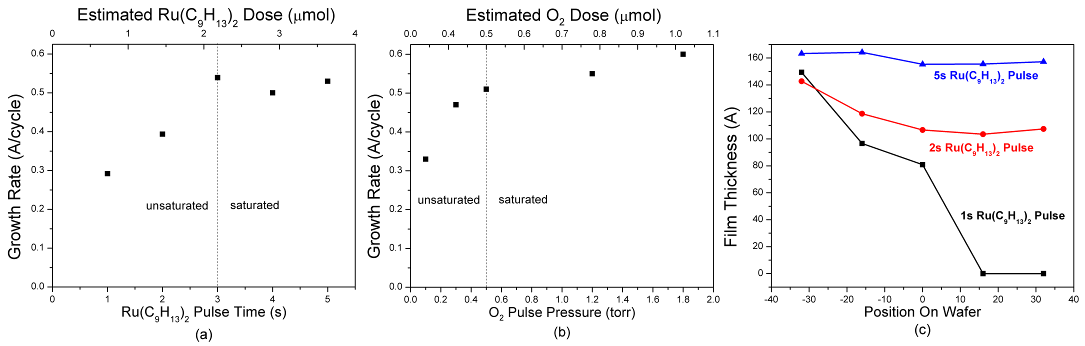

Figure 6. Growth rate of Ru film as a function of (a) $Ru(C_9H_{13})_2$ pulse time and (b) O_2 pulse pressure. While holding the oxygen pulse at 1.2 Torr, the cross wafer thickness as a function of position on the wafer (panel c) for two points in the unsaturated region and one in the saturated region was studied. The black squares represent measurements made for $Ru(C_9H_{13})_2$ pulse times of 1s, the red circles for pulse times of 2s. The blue triangles show fully saturated conditions at 5s pulse times.

adsorbed molecules fully saturate the surface, resulting in a self-limited half-reaction characteristic of ALD.

The effect of reactant depletion in the under exposure regime is clearly in evidence as revealed by the use of the cross-flow reactor configuration, as shown in Figure 6c, the film thickness across the wafer drops along the direction of the flow for 1s (black squares) and 2s (red circles) $Ru(C_9H_{13})_2$ exposures, clearly indicating an incomplete saturation of the surface sites across the wafer. O_2 pulse time and pressure were held constant at 1s and 1.2 torr during these measurements. Saturated ALD dose conditions are seen for 5s pulses (blue triangles), across-wafer uniformity is greatly improved, with a non-uniformity of less than 5% on SiO_2 substrates and less than 2% on TiO_2-coated samples.

Results in Figure 6b suggest the possibility that at high O_2 partial pressure, i.e., >0.5 μmol, only a pseudo-saturation occurs, with the GPC increasing slightly beyond 0.5 Å/cycle with increasing pressure. The absence of definitive saturation is likely a result of the methodology used to control the O_2 dose in this case. Rather than varying the pulse time under fixed flow conductance, which is a more common technique, higher oxidant doses were achieved by increasing the O_2 flow rate and thus partial pressure for a fixed O_2 pulse time. Under such conditions, it has been reported that a higher conversion of the surface sites caused by the higher partial pressure of the oxidant can be achieved, leading to a higher GPC [65, 66]. Based on the data from Figure 6b, optimized exposure conditions for O_2 correspond to ~0.8 μmol (or 1.2 Torr pressure pulse).

As seen in Figure 7, the temperature process window for the $Ru(C_9H_{13})_2 – O_2$ ALD Ru process was characterized by monitoring the GPC as a function of substrate temperature from 200 to 350°C under optimized exposure and purge conditions, i.e. 2.2 and 0.8 μmol exposures for $Ru(C_9H_{13})_2$ and O_2 respectively, with 15s purges between each. These data show a clear ALD process window between 250°C and 300°C where the GPC remains constant at 0.5 Å/cycle. This represents an improvement over some of the more common precursors. The sharp drop in the growth rate observed at temperatures above 300°C (with zero growth at temperatures approaching 350°C) most likely reflects a combination of thermal decomposition of the precursor, which is consistent with the DSC data shown in Figure 4b, and thermal desorption of the molecule from the substrate surface.

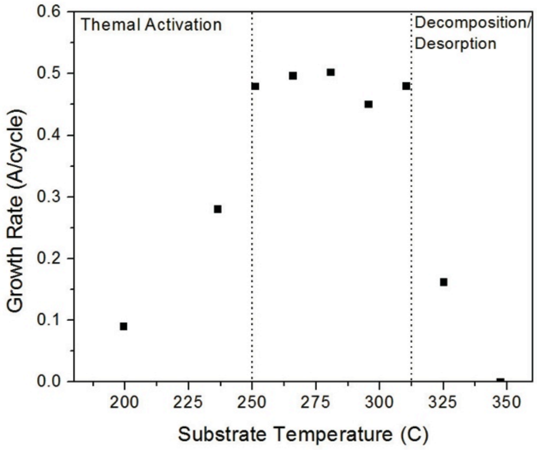

Figure 7. Temperature window showing the growth rate as a function of substrate temperature. A stable window is seen between 250 °C and ~312 °C. Beyond this temperature, some combination of precursor decomposition and thermal desorption from the substrate lead to a sharp decrease of the growth rate.

To investigate the nucleation kinetics of this Ru ALD process, we carried out the optimized ALD process on TiO_2 and Al_2O_3 coated surfaces as well as on the SiO_2 and on H-terminated Si surfaces. All of the substrates were held at 270°C, well within the temperature window shown in Fig. 4, and Ru films were deposited for 50, 100, 250, and 500 cycles. As can be seen in Fig. 5, SiO_2 surfaces exhibit the shortest nucleation delays, followed by TiO_2 and to a lesser degree H-terminated Si. All of these substrates showed short nucleation delays, none larger than 50 cycles. Post-process ellipsometry measurements indicate a low 2-5% non-uniformity across the wafer. Four-point probe sheet resistance measurements of 25 nm Ru films indicate a 20μΩ-cm resistivity.

Ru ALD deposition on Al_2O_3 reveals a significant nucleation delay, 250 cycles to initiate growth. As presumably all of the oxide materials involved surfaces terminated with hydroxyl groups, we infer that the nucleation dynamics are not solely

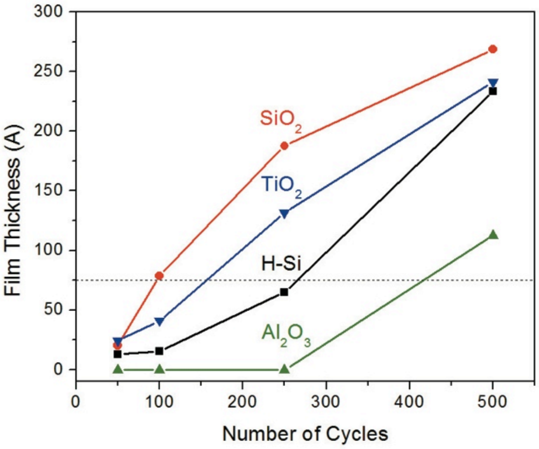

Figure 8. Film thickness as a function of total number of cycles for four different substrates, showing low nucleation retardation for SiO_2, TiO_2, and H-terminated Si. Data for Al_2O_3 shows a significantly higher nucleation barrier, requiring at least 250 cycles before film growth begins. Comparing film thickness data to XRD data (Figure 6) shows that films less than ~75 Å (dotted line) are amorphous.

driven by the nature of the surface groups available for adsorption. It is noteworthy that nucleation, on H-terminated Si is faster than on the alumina surface.

2.3.3 Material Characterization

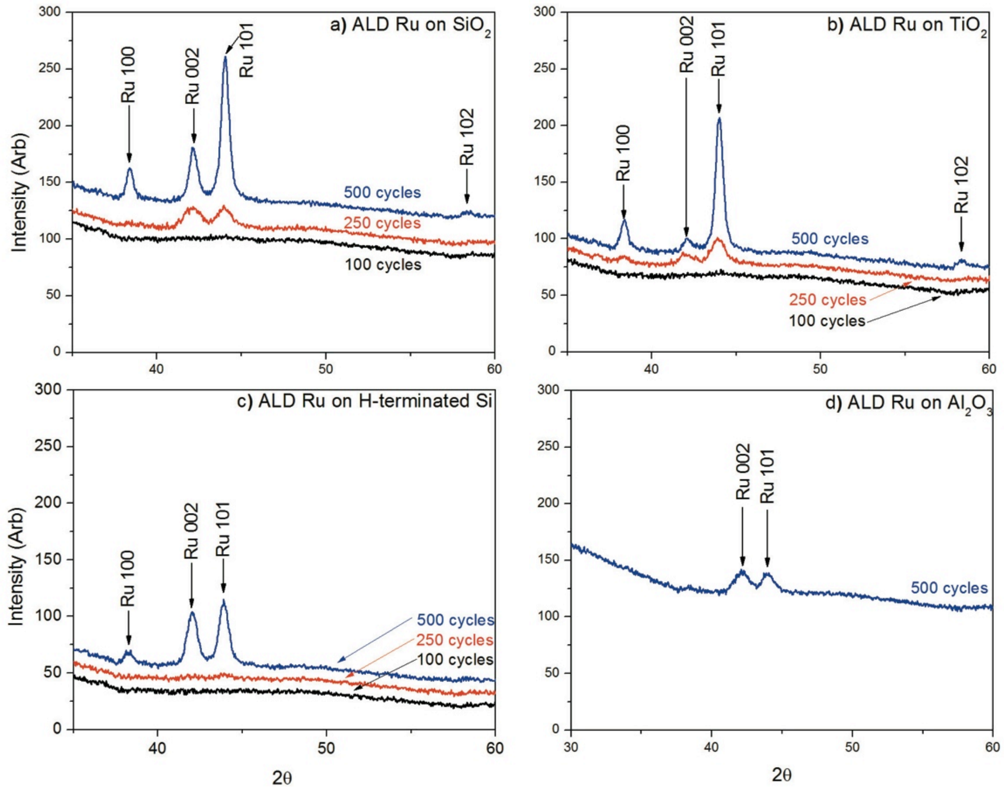

Figure 9. X-ray diffraction (XRD) data for films grown on four different substrates (as noted in top right corner of each panel). Films are all polycrystalline and show increased peak intensity as the thickness increases. Each substrate had three different thicknesses deposited on it, as noted by the number of cycles (blue corresponds to 500 cycles, red to 250 cycles, and black to 100 cycles).

Results from XRD (Figure 9) and SEM (Figure 10), show that the deposited films are nano-grained polycrystalline films comparable to previously published results with Cp and tris-β-diketonate based chemistries [48, 67]. Figure 9 shows the diffraction pattern for films deposited on four different substrates; SiO_2, TiO_2, H-terminated Si, and Al_2O_3, at three different thicknesses, except for Al_2O_3 which was only measured at 500 cycles (or ~100 Å). Results for these data are reported in terms of the number of cycles rather than thickness due to differences in thickness from slow or delayed nucleation. The observed diffraction peaks for Ru (100), (002), (101), and (102), with (102) only being seen on SiO_2 and TiO_2, appear comparable to other published results [48, 61, 67-69]. Peak intensities depend on overall film thickness rather than on the nature of the substrate.

Films grown on SiO_2, TiO_2, and Si only show crystallinity at thicknesses over ~75 Å. As can be seen by comparing results shown in Figure 8 to the XRD data shown in Figure 9. XRD for the Al_2O_3 substrates was only performed for 500 cycles since nucleation was strongly delayed in this case (Figure 8), leading to low Ru coverage for smaller number of cycles (see SEM results below). Using the Debye-Scherrer equation the average grain size over all orientations, except the (102), was calculated for each of the substrates giving the following values; on Si 13.11±0.49nm, on SiO_2 16.57±2.65nm, on TiO_2 16.49±0.88nm, and on Al_2O_3 9.81±1.24nm.

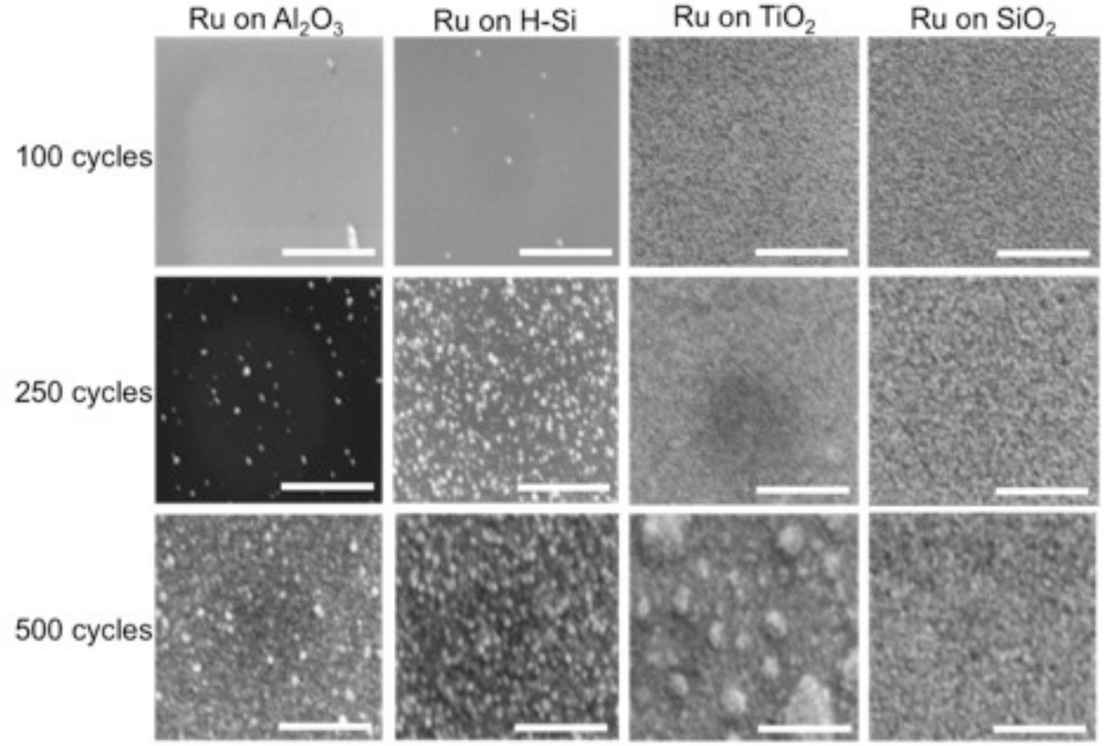

Figure 10. SEM images showing nucleation behavior of $Ru(C_9H_{13})_2$ on the four different substrates used: Al_2O_3, H-terminated Si, TiO_2, and SiO_2. Continuous films show nanograin structure. Scale bar represents 500 nm.

SEM images for ALD Ru on the four substrates at 100, 250, and 500 cycles are shown in Fig. 7, corresponding to the conditions for the XRD results in Fig. 6. These images are consistent with the average grain size for the four cases as calculated by the Debye-Scherrer equation.

2.3.4 Electrical Characterization

Figure 11 shows the thickness dependent (Figure 11a.) and temperature dependent (Figure 11b) conductivity, and the temperature coefficient of resistivity (TCR) (Figure 11c), extracted from the data in Figure 11(b), for these ultrathin Ru films. Conductivity of a film, σ_f, is given as $\sigma_f=n_A e\mu_{net}$, where n_A is the number of charge carriers, e the electron charge, and μ_{net} is the effective mobility of the charge carriers. First we consider the thickness dependent (at RT) data shown in Figure 11a. A ~5x decrease in conductivity is seen from ~38x10^3 S cm^{-1} for a 24 nm film to ~8x10^3 S cm^{-1} for a 5 nm film. Conductivity further drops to ~46 S cm^{-1} for a 4 nm, a ~700x decrease. Below this thickness (3 nm) films were completely

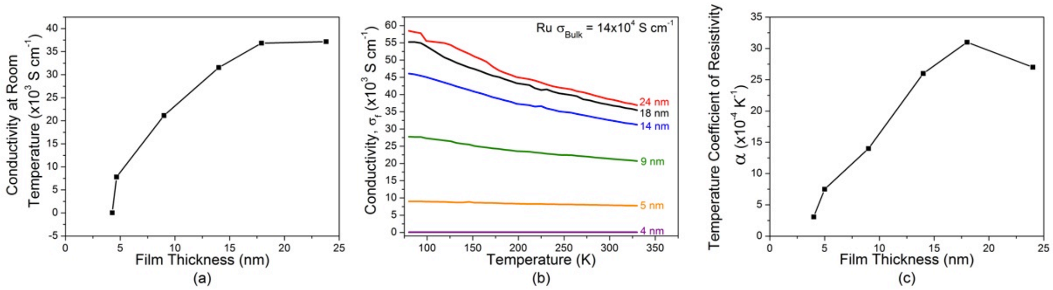

Figure 11. Conductivity of ultrathin Ru films as a function of film thickness (a), temperature (b), and the TCR (c) extrated from the data shown in (b).

insulating, beyond the measurement capabilities of the instrument used (>10^7 Ωcm) [70].

This trend is further illustrated in the temperature dependent data through the slopes of the individual curves shown in Figure 11b. Films 14 nm and above show temperature-dependent conductivity as expected from normal electron-phonon scattering in metals. For the thickest film (24 nm) we see a ~2x decrease in conductivity from ~58x10^3 S cm^{-1} at 80K to ~30x10^3 S cm^{-1} at 340K. However, for film thicknesses < 14 nm the slope flattens out indicating a reduced temperature dependence. The thinnest film (4 nm) barely shows a change in conductivity as a function of temperature with a value of 48 S cm^{-1} at 80K only decreasing to 45 S cm^{-1} at 340K.

To better understand the temperature effects seen in Figure 11b the TCR was calculated for each film thickness using equation 1 and the results are shown in Fig. 11(c).

$$\alpha = \frac{1}{\rho_o}\left(\frac{\partial \rho_f}{\partial T}\right) \qquad (1)$$

Where ρ_o and ρ_f are the bulk (7 μΩ cm)[33] and film resistivities respectively and T is the temperature. The TCR is a measure of how temperature, i.e. electron-phonon scattering, affects the conductivity of a material. For these data we see a substantial decrease, ~9X, from ~27x10^{-4} K^{-1} for a 24 nm film to ~3x10^{-4} K^{-1} for a 4 nm film to, showing the sensitivity of σ_f to temperature as the thickness of the Ru film drops considerably. From these data it can be concluded that temperature dependent electron-phonon scattering mechanisms become less dominant as the films become thinner consistent with previously reported work [71].

Therefore to explain the marked decrease in conductivity as a function of film thickness seen in Figure 11a and 11b we consider the size effect limit described by Mayadas-Shatzkes (MS) theory [72, 73]. This theory addresses transport in spatially constrained geometries, where film thickness or grain size is small enough to dominate scattering and transport of electrons. MS theory predicts decreasing electrical conductivity with decreasing thickness as a result of (1) increased surface/interface scattering events and (2) grain boundary scattering through the following equation:

$$\sigma_f = \sigma_o \left[1 + \frac{3l_o(1-p)}{\delta} + \frac{7}{5}\frac{l_o R}{d(1-R)}\right]^{-1} \qquad (2)$$

Here σ_f is film conductivity, σ_o is bulk conductivity, p is the specular reflection parameter, l_o is the mean free path (MFP) of charge carriers in a grain, δ is the film thickness, d is the average grain size, and R is the reflection coefficient at grain boundaries[72, 74]. The ability of ALD to create and control the thickness and properties of very thin metal layers provides a valuable opportunity to compare experimental data with MS theory.

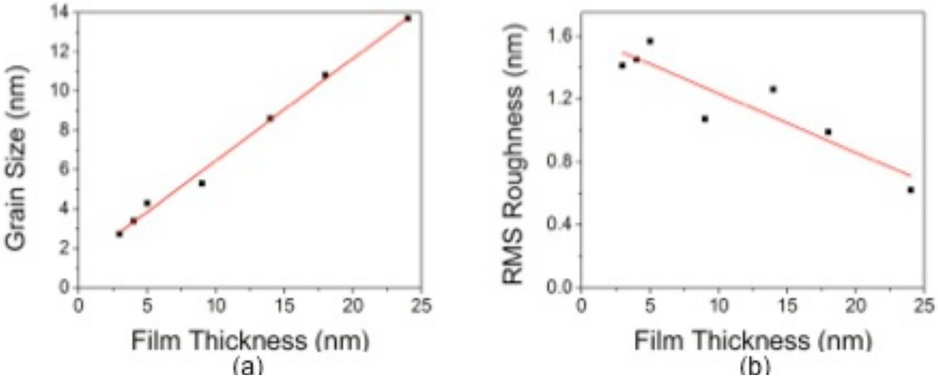

Figure 12. Summary of AFM results for ALD Ru films with the grain size (a) and RMS roughness (b) shown as a function of film thickness.

To understand the implications of MS theory on these data we must first understand how grain size changes as a function of film thickness. As discussed in Chapter 2.3.3, Ru films grown with this process go through a nucleation and growth process leading to a variation in grain size as function of film thickness [75, 76]. Figure 12 shows the grain size (Figure 12a) and RMS roughness (Figure 12b) as a function of film thickness. A roughly linear decrease in RMS roughness is seen as a function of film thickness (Figure 12b), consistent with previously reported ALD processes [77]. Furthermore, a clearly linear increase in grain size is seen as a function of film thickness (Fig 2a) and is consistent with grain sizes calculated from from XRD data shown in Figure 9 [76]. From these results we see at very low film thickness, i.e. 3 and 4 nm, RMS roughness values approach the thickness of the films, 1.6 and 1.4 nm respectively. Thicker films are considerably smoother with RMS roughness values dropping to 0.6 nm for the 24 nm film.

Using the results for grain size (Figure 12a) and an estimated MFP (l_o) of 10 nm [78], two parameters are left to determine in equation 2, namely R and p (even though it should be noted that MFP in polycrystalline metal films can be difficult to define [79]).To calculate R three different values of p were chosen representing complete specular reflection (p=1), complete diffuse scattering (p=0), and an intermediate value (p=0.5). The grain boundary reflection coefficient R was calculated and optimized by reducing the difference between measured and calculated values of σ_f using equation 2. The results of these calculations are shown in Figure 13.

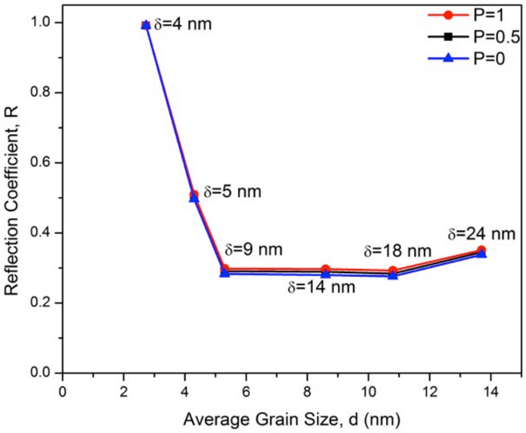

Figure 13. Reflection coefficient as a function of grain size, with corresponding film thickness (δ) noted next to each data point. Three calculations of the reflection coefficient (R) were made using different values of the specular reflection parameter (p). In all three cases the reflection coefficient follows the same trend; decreasing as a function of thickness and becoming constant at ~0.3 showing grain boundary scattering dominates for thinner films while interface/surface scattering become more dominant for thicker films.

Two conclusions can be gathered from this figure. First, very little difference is seen for the R calculated for different values of p. Second, R decreases for thicker films saturating at a value of ~0.3. This trend indicates that grain boundary scattering is more important for extremely thin films (4 and 5 nm) while surface/interface scattering becomes more dominant as the films become thicker, similar to results published for Au and Al [80].

To understand these results film growth through nucleation must be considered. Nuclei grow in size until they begin to coalesce into crystallites of energetically favorable crystal orientations through a number of possible mechanisms [81]. Crystallites continue to grow and impinge on one another, sometimes merging, but also creating grain boundaries. During the transition from individual crystallites to a continuous granular film the dominant conduction mechanisms change. The data shown here reflect this change.

By considering the results shown in Figures 11-13 a complete description of the decrease in conductivity for these films can be presented. Figure 11(b) and 11(c) show that electron-phonon interactions become less dominant as film thickness decreases and can therefore not explain the decrease in conductivity seen at lower thicknesses. For film thickness below ~14 nm the TCR drops significantly corresponding to a drop in conductivity seen in Figure 11(a). Although electron-phonon interactions may still have some influence, geometrical constraints are beginning to play a significant role through scattering at surfaces/interfaces. This trend continues for the 9 nm and 5 nm films. To quantify the role of these geometrical constraints, R was calculated through MS theory (Figure 13) and shown to stay constant at ~0.3 for films greater than 9 nm. Below 9 nm, however, R begins to increase as grain boundary scattering begins to have a greater contribution to the decreased conductivity. At 4 nm an incredibly high R of ~0.99 is seen, which most likely represents the limit of what MS theory can describe. Individual crystallites may not be in complete contact, though close enough to allow mechanisms such as percolation or tunneling [82]. Finally at 3 nm the films become completely insulating due to an incomplete film, this can be seen in Figure 12a and 12b where RMS roughness is more than half the film thickness.

2.4 RuO_2 ALD

During the development of the Ru ALD process it was observed that if the oxygen partial pressure was increased dramatically during the reaction RuO_2 rather than Ru was deposited. This chapter discuss the development of this process and represents the *first fully developed and characterized RuO_2 ALD processs.*

2.4.1 RuO_2 ALD Literature Review

The RuO_2 ALD reports are summarized as follows. Using bis(cyclopentadienyl)ruthenium ($RuCp_2$), a significant increase in the growth rate per cycle (GPC) from 1.2 Å/cycle to 3.2 Å/cycle was seen as a function of increased oxygen partial pressure and was accompanied by an increase in film resistivity [83]. Much more prevalent has been the use of bis(ethycyclopentadienyl)ruthenium ($Ru(EtCp)_2$) where several reports have noted an increase in the GPC and resistivity of the resulting films. Characterization through x-ray diffraction (XRD) and x-ray photoelectron spectroscopy (XPS) showed that these films were RuO_2, with reported growth rates varying between 1.4 and 1.6 Å/cycle [61, 83-86]. A modified ALD process, in which a constant partial pressure of O_2 was held during the reaction, also used $Ru(EtCp)_2$ and resulted in RuO_2 films [87]. An in-situ IR-spectroscopy study reported the formation of RuO_2 using cyclopentadienyl ethylruthenium dicarbonyl ($Ru(Cp)(CO)_2(Et)$) after a nucleation period of 1-5 cycles where only Ru particles were observed [88]. This study reported a GPC range between 1.5-3 Å/cycle, but only studied out to 25 cycles. A liquid injection ALD process using bis(2,2,6,6-tetramethyl-3,5-heptanedionato)(1,5-cyclooctadiene)ruthenium), $Ru(thd)_2(COD)$, dissolved in iso-octane, reported a GPC of 6.6 Å/cycle for processes between 20 and 60 cycles [89]. Another report used Ru(od)$_3$/*n*-butyl acetate solution to deposit Ru onto CNTs which were then annealed at 500°C in O_2, which oxidized the film and removed the CNT template [90]. Finally our previous results using bis(2,6,6-trimethyl-cyclohexadienyl)ruthenium also noted that if the partial pressure of O_2 was increased a phase change was seen [76]. We emphasize that despite these numerous observations of RuO_2 growth during Ru-based processes no fully optimized parameters (i.e. precursor and oxidant dosage saturation curves, as well as, temperature window and resulting film properties) have been published. At table of Ru-based precursors with mention of RuO_2 deposition may be found in Appendix 2.

2.4.2 RuO_2 ALD Process Parameters

In order to observe evidence for the self-limited chemisorption reaction characteristic of an ALD process, the GPC was monitored as a function of $Ru(C_9H_{13})_2$ dose, O_2 dose, and substrate temperature. The results for these experiments are shown in Figure 14(a-c). First we consider the $Ru(C_9H_{13})_2$ dose. While holding the O_2 pulse time at 30s, the $Ru(C_9H_{13})_2$ pulse was varied from 2-20s the results of which are shown in Figure 14(a). Saturated ALD growth rates are seen for pulses 5s and longer giving a growth rate of 0.4 Å/cycle. Next the $Ru(C_9H_{13})_2$ pulse was held constant at 10s, well within the saturated regime, and the O_2 pulse time was varied between 4 - 30s with the results shown in Figure 14(b). Once again a saturated GPC of 0.4 Å/cycle is seen, for pulse times 15s and longer.

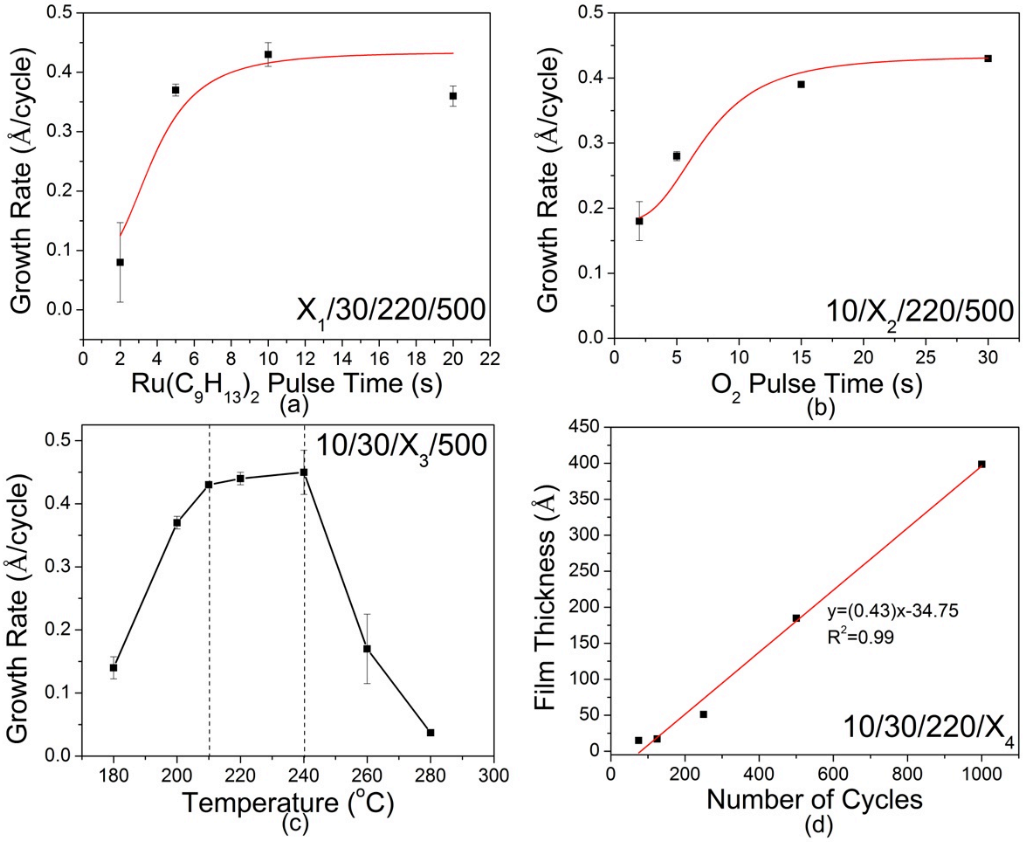

Figure 14. ALD process parameters, $Ru(C_9H_{13})_2$ pulse time/O_2 pulse time/temperature/number of cycles denoted as $X_1/X_2/X_3/X_4$ in each figure. (a, b) show the saturation curves for $Ru(C_9H_{13})_2$ and O_2 respectively, each showing a saturated growth rate of ~0.4 Å/cycle . (c) The temperature window using the optimized process parameters. (d) Film thickness versus number of cycles confirming the saturated growth rate of 0.43 Å/cycle observed in (a) and (b) and also showing a nucleation period of 70-80 cycles.

Figure 14(c) shows the temperature window for the $Ru(C_9H_{13})_2$ –O_2 ALD RuO_2 process as a function of substrate temperature from 180°C to 280°C under the above optimized exposure and purge conditions (i.e. 10s $Ru(C_9H_{13})_2$, 30s O_2, and 5s Ar purge). These data show a clear temperature window between 210°C and 240°C where the GPC remains constant at 0.4 Å/cycle. The sharp drop in the GPC observed for temperatures below 210°C and above 240°C are generally considered to be characteristic of an ALD processes, where there is an incomplete reaction at lower temperatures (here, below 210°C) and where thermal desorption of the molecule and/or a loss of surface species are occurring at higher temperatures (here, above 240°C) [45].

To understand the nucleation kinetics of this RuO_2 ALD reaction, the film thickness was measured as a function of cycle number, also using the optimized process parameters. The substrate temperature was held at 220°C, well within the temperature window, and films were deposited at 75, 125, 250, 500, and 1000 cycles, the results are shown in Figure 14(d). A reasonably linear fit is obtained, with two important consequences. First the slope of the fit gives a GPC consistent with the rest of the process parameters shown in Figure 14(a-c), with a value 0.43 Å/cycle, and second, by extrapolating the fit through the x-axis, the nucleation period can be estimated as ~70-80 cycles.

2.4.3 Material Characterization

To determine the crystal structure, thick films (1000 cycles, ~40 nm) were deposited on SiO_2 and XRD patterns were obtained with the results shown in Figure 15. It is clear that these films are poly-crystalline and nano-grained. The dominant peaks, as discussed, are the overlapping RuO_2(110) and RuO_2(101), however smaller peaks are visible for the RuO_2(011), RuO_2(211), RuO_2(002), and RuO_2(112) reflections. More importantly, no

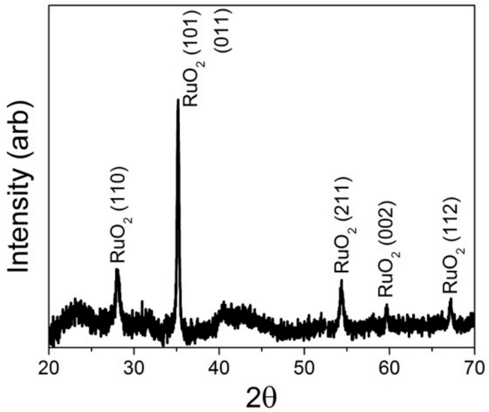

Figure 15. X-ray diffraction pattern of a ~40 nm RuO_2 ALD deposited on SiO_2. The as-deposited films are polycrystalline with dominant peak seen for (101) and (011). Smaller peaks are seen for (110), (211), (002), and (112) crystal directions.

peaks are seen for metallic Ru, confirming that only the oxide phase is present.

To study the local structure thick films (1000 cycles, ~40 nm) were again deposited on SiO_2 substrates. Raman spectroscopy was conducted on these samples and was compared to a commercially purchased RuO_2 powder (Sigma-Aldrich) as well as metallic ALD Ru films, which were deposited with the same precursor using our previously published process, the results of which are shown in Figure 3 [76]. The spectrum for crystalline RuO_2 has three modes, E_g at 528 cm^{-1}, A_{1g} at 644 cm^{-1}, and B_{2g} at 716 cm^{-1} [91]. All three modes are visible in our results. In comparison to the purchased powder a nearly 1:1 overlap between the RuO_2 powder peaks and the ALD RuO_2 films peaks can be seen. Only small versions of the RuO_2 peaks, due to native oxide growth, are seen on the ALD Ru films.

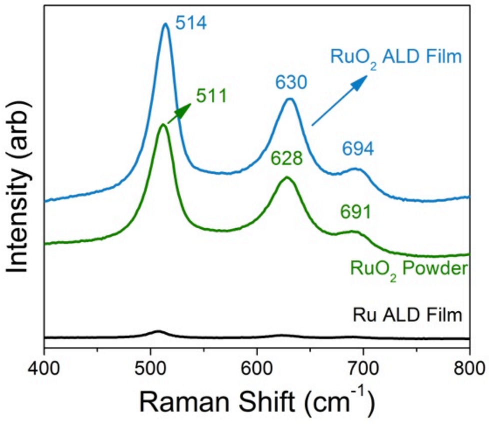

Figure 16. A comparison of Raman spectra for RuO_2 by ALD, commercial RuO_2 powder, and Ru by ALD showing a nearly 1:1 agreement. Small peaks due to native oxide growth are seen for the Ru ALD film but otherwise show the two ALD processes are distinct.

Film morphology was obtained through AFM with both the RMS roughness and grain size being monitored as a function of film thickness. The results for these experiments are shown in Figure 4. Both RMS roughness and grain size can be seen to increase nearly linearly as a function of film thickness. For the thinnest films studied corresponding to 75 cycles or ~1.5 nm a RMS roughness of 0.4 nm is seen. The grain size for these films was calculated (see experimental section) to be 3.06

nm. The RMS roughness and grain size continues to increase and after 1000 cycles the RMS roughness is seen to be 2.86 nm and corresponds to a grain size of 18.2 nm.

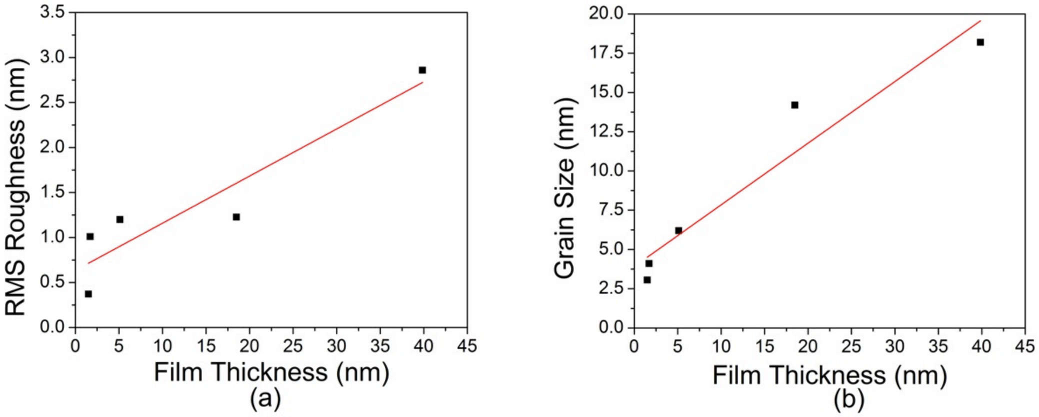

Figure 17. AFM results showing a nearly linear increase in RMS roughness and grain size as a function of film thickness.

2.5 A comparison of reaction mechanisms

In the prior $RuCp_2$ work sub-surface oxygen was shown to play a critical role in the reaction, through oxidation of $RuCp_2$ into CO_2 and H_2O during both the $RuCp_2$ pulse and the O_2 pulse, leading to film growth during both steps. Though not the focus of this paper we did observe similar reaction species with a downstream mass spectrometer for the associated Ru process. Furthermore, several studies of O adsorption on Ru surfaces have shown that up to 10 ML of O can be adsorbed in subsurface regions at room temperature (RT) [92-95]. Aaltonen *et al* showed for Ru ALD from $RuCp_2$ and O_2 that the subsurface oxygen was not only required to complete the reaction but that it was also entirely consumed, leading to Ru films [49]. Using the same process and studying the effect of oxygen concentration, it was noted that when the O_2 partial pressure was increased during the reaction the resulting film had a higher resistivity and XPS showed the films were RuO_x [83]. Furthermore, recent in-situ infrared spectroscopy results using the precursor $Ru(Cp)(CO)_2Et$ and O_2 have shown that the first few cycles of the process do in fact deposit Ru, but once enough Ru is available for O adsorption the process begins to deposit RuO_2[88]. Similar results have been reported for processes using $Ru(EtCp)_2$ [61, 83-85].

From these literature studies it would seem that the mechanism by which Ru or RuO_2 is deposited depends entirely on the amount of subsurface O available. However, it was also shown that the activation energy for desorption of an O adatom decreases with increasing temperature [94]. Despite the fact that this report uses different precursors than those discussed here, it appears that this reaction pathway is common for several Ru-based precursors. Therefore, we infer that this reaction mechanism is a rather delicate balancing act of controlling the concentration of subsurface O, including for the RuO_2 ALD process reported here.

This RuO_2 ALD process shows a lower GPC and lower temperature window than its associated Ru ALD process. Considering the latter point first, while several reports have noted RuO_2 at higher temperatures, there have not been any systematic temperature studies that compare the deposition of Ru and RuO_2 using the same precursors and therefore no conclusions can be gathered from the literature to elucidate reaction mechanics of the process reported here. Concerning the lower GPC we expect that the balance between adsorption/desorption of subsurface O is the most likely cause, but without further in-situ experiments such as mass spectroscopy or the use of a quartz crystal microbalance the authors recognize that these conclusions may be speculation.

2.6 Chapter Summary

In this chapter two ALD processes were shown using the novel precursor, bis(2,6,6-trimethyl-cyclohexadienyl)ruthenium. The first process discussed was for Ru, which showed a stable growth rate of 0.5 Å/cycle, and a shorter nucleation on most substrates, as compared to those chemistries available in the literature. Material and electrical characterization confirmed that pure Ru was produced and showed a thickness dependent conductivity.

When the oxygen partial pressure was increased RuO_2 rather than Ru was deposited. A stable growth rate of 0.4 Å/cycle was shown and the two processes were discussed in terms of O_2 partial pressure.

Chapter 3: Thin Film RuO_2 Li-ion Batteries

3.1 A Brief Review of Thin Film Batteries

The majority of thin-film batteries have been fabricated using standard materials used in commercially available battery systems such as $LiCoO_2$ and $LiMn_2O_4$ as cathodes and lithium metal as an anode [96, 97]. Furthermore they are almost always solid-state systems and use the now standard solid-state electrolyte lithium phosphorous oxynitride better known as lipon. Most of the work concerning these materials including the fabrication process has been conducted at Oak Ridge National Labs (ORNL) where a number of detailed review papers have been published [96-102]. Physical deposition methods such as rf magnetron and evaporation were used to fabricate the cells. Details of these processes can be found in the reviews cited above and through the citations there in.

While this section does use thin-films of RuO_2 the purpose of the work was not to add to the thin-film literature nor to fabricate thin-film batteries with any particular application in mind, but rather to understand the behavior of an often mentioned but little studied material.

RuO_2 is in a class of materials referred to as the conversion electrodes whose reversible reaction with lithium can be generalized as follows:

$$M_aX_b+(bn)Li \leftrightarrow aM+bLi_nX \qquad (3)$$

where M can be Ti, V, Cr, Mn, Fe, Co, Ni, Cu, Mo, W, or Ru, X can be O, S, N, P, or F, and n is the formal oxidation state of X [103]. When RuO_2 is inserted into the reaction it is written $RuO_2+4e^-+4Li^+ \leftrightarrow Ru^0+2Li_2O$ [39]. As mentioned in Chapter 1.4 a few papers exist in the literature using RuO_2 as a battery material. In these papers, however, commercially available RuO_2 powder, carbon black, graphite, and polyvinylene difluoride were mixed in a weight ratio of 10:1:1:1 and then pasted onto a Ti foil [39]. The first cycle was reported to have a coulombic efficiency of 98%, however this mixture would fail after 3 cycles. Follow-ups to this report used nano-sized powders mixed with similar binders and showed enhanced capacity of amorphous materials and did excellent work on the nano-ionic behavior of this material [40, 44, 104, 105]. None these papers, however, studied cyclability or the more practical aspects of this material. Therefore, this work represents the first electrochemical characterization of pure RuO_2 as well as the first cycling data and attempt to understand the degradation mechanisms.

3.2 Fabrication of RuO_2 ALD Batteries

To investigate the electrochemical properties of ALD RuO_2 half-cells versus Li/Li$^+$ were fabricated using a standard 2032 coin cell whose assembly is shown in Figure 15. Stainless-steel discs were degreased by sonication in a 1:1 mixture of isopropyl alcohol and acetone for 10 mins and blown dry with N_2. They were then weighed before and after deposition using a Mettler Toledo XS105 dualRange microbalance with a resolution of 1 µg. 150 ± 7 µg (2000 cycles) of RuO_2 was deposited using the

Figure 18. Schematic of 2032 coin cell fabrication showing the casings, spring, spacer and relative positions of cathode, anode and separator.

Figure 19. Photographs of (a) a RuO_2 coated stainless steel disc and (b-c) a completed coin cell.

optimized parameters. RuO_2 coated stainless steel discs were baked overnight at 100°C before cell assembly. Coin cells (2032) were fabricated in a dry Ar filled glove box with lithium (Sigma Aldrich) as the counter electrode, a Celgard separator (Celgard 3501), and 1M $LiPF_6$ in a 1:1 mixture of ethylene carbonate (EC) and diethyl carbonate (DEC) (Novolyte Technologies) as the electrolyte. An Arbin BT-2000 multichannel battery test station was used for galvanostatic, rate capability, and life cycle testing. Electrochemical impedance spectroscopy was done with a Bio-Logic VMP3 using the same coin cell configuration and fabrication described above.

3.3 Electrochemical Characterization

The first cycle discharge/charge curves for different C rates are shown in Figure 20(a). As expected the highest capacity is seen for the slowest C rate of C/100, namely ~1450 mAh/g, which is slightly higher than the stoichiometric theoretical capacity of 1410 mAh/g. As mentioned in Chapter 3.1, the expected lithiation reaction is, $RuO_2+4e^-+4Li^+ \leftrightarrow Ru^0+2Li_2O$, which produces two species in the fully discharged state, Ru and Li_2O. Experiments with micron sized RuO_2 powders have confirmed that after full discharge the Ru becomes nanosized particles in a Li_2O matrix [39]. Other work has shown that extra Li^+ can be stored at the Ru/Li_2O

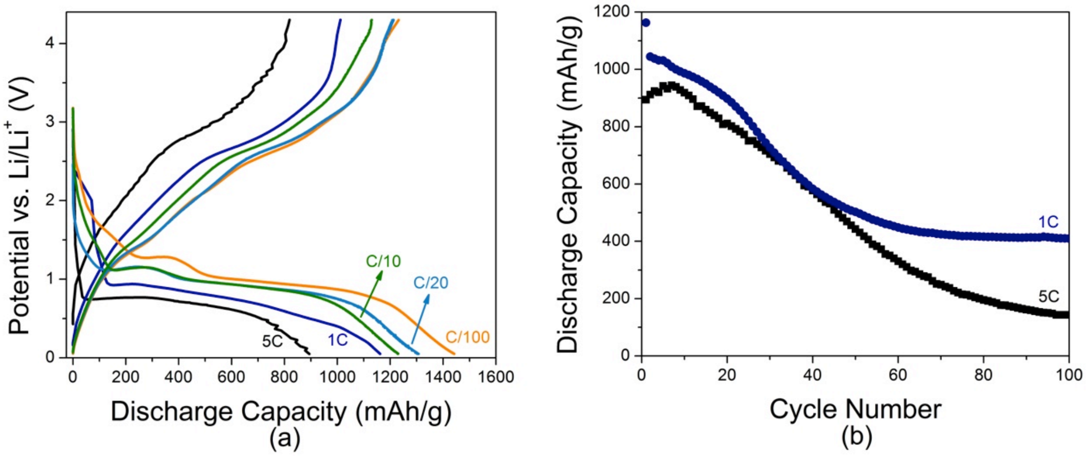

Figure 20. Electrochemical characterization of RuO_2 ALD fabricated into a standard coin cells. First cycle discharge capacities, (a), showing a high capacity 1450 mAh/g at C/100, 1300 mAh/g at C/20, 1200 mAh/g, 1100 mAh/g at 1C, and 900 mAh/g at 5C. Plateaus corresponding to $Li_{0.86}RuO_2$, seen at ~1.25V for C/100 and ~1.1V at C/20 and C/10, $Li_{1.2}RuO_2$ at ~1V, and a matrix of Ru/Li_2O at 0.05V. The cyclability of these electrodes is shown in (b) for 1C and 5C. The capacity is seen to drop to ~400 mAh/g after 40 cycles for 1C. At 5C the capacity is seen to increase for the first 10 cycles and then falls to ~150 mAh/g.

interface [105]. We therefore attribute the excess capacity measured at this slow discharge rate to lithiation at the Li_2O/Ru interface, as suggested in other conversion electrode systems.

Faster C rates show a decline in capacity, though it should be noted that all of the capacities for the ALD RuO_2 are higher than the standard carbon negative electrode. At C/20 the capacity is 1300 mAh/g, decreasing to 1200 mAh/g at C/10. All three of these curves (C/100, C/20, C/10) show similar structure with two plateaus visible. The first small plateau is seen at 1.25V for C/100 and appears at 1.1V for the C/20 and C/10 rates. According to the previously published RuO_2 powder data this first plateau corresponds to $Li_{0.86}RuO_2$ [40]. The second and larger plateau visible at ~1V for C/100, C/20, and C/10 corresponds to $Li_{1.2}RuO_2$ according to the same reference. Finally the tail of the curves, which dips down to 0.05V, correspond to the fully lithiated phase where the reaction has gone to completion and, as mentioned, has been shown to be a matrix of Ru nanoparticles in a Li_2O matrix. Generally these curves compare well to those reported in the literature, though an exact comparison is not possible since no pure RuO_2 results have been reported [39, 40].

At the fastest two rates studied, 1C and 5C, the capacity of the films decreases and the curve's shape also changes. The 1C films show a capacity of over 1100 mAh/g while the 5C results decreases to 900 mAh/g. The plateaus corresponding to the $Li_{0.86}RuO_2$ phase are no longer visible and the large plateau for the $Li_{1.2}RuO_2$ phase gradually slopes into the tail corresponding to the Ru/Li_2O mixture. We conclude that the intermediate phases are only possible when the films are discharged slowly enough for them to react and remain stable, behavior which has been seen before for intercalation electrodes such as TiO_2 [106].

Figure 20b shows the cyclability of the ALD RuO_2 films at 1C and 5C. The 1C data shows a quick decrease in capacity from 1200 mAh/g to 1000 mAh/g after the first cycle. After the first two cycles, the capacity steadily declines and stabilizes at ~400 mAh/g after 60 cycles. The 5C data shows an increase in capacity for the first 10 cycles after which it steadily declines, never truly saturating but reaching a capacity of ~150 mAh/g after 100 cycles. It may be that for the higher rate (5C) in the first few cycles not all of the mass of ALD RuO_2 is used, and that as the battery is cycled more of the material becomes active, resulting in an increase in capacity. After this initial increase the capacity decays similar to the 1C battery. No cyclability data are available in the literature for comparison.

3.4 Degradation Mechanisms

The capacity degradation can be partially understood through the dramatic structural changes seen in the SEM images in Figure 21 (a-d). The as-deposited films

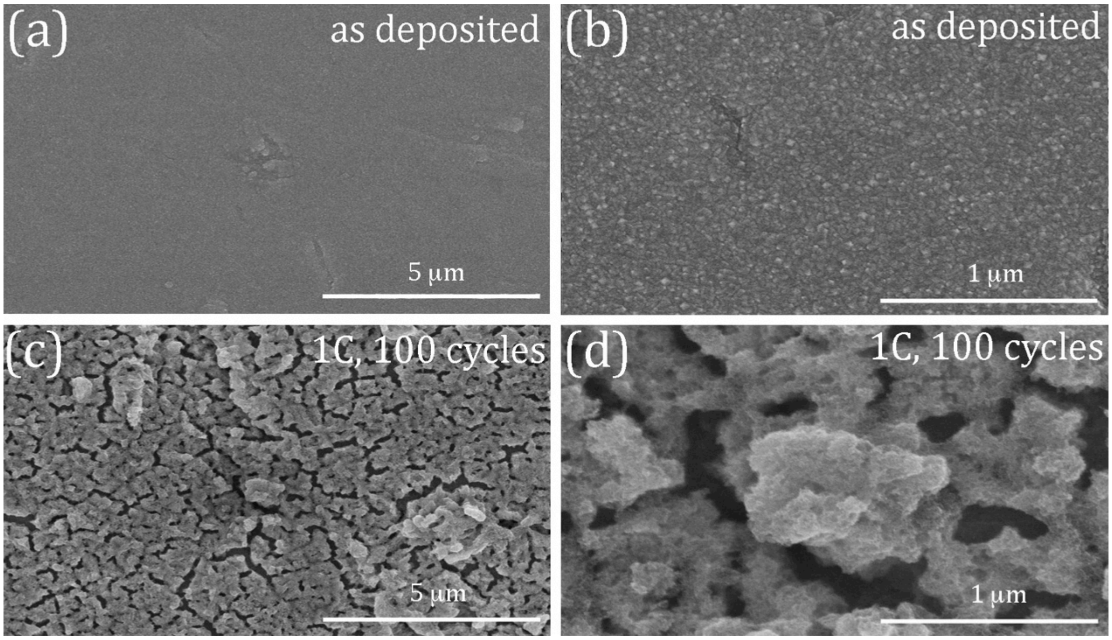

Figure 21. SEM images of RuO_2 ALD films deposited on stainless steal discs before and after cycling, (a) and (b) show high and low magnification images of the as deposited films. (c) and (d) show the same two scales after the batteries were cycled 100 times at 1C. These images show significant morphological changes and degradation after cycling.

are shown in Figure 20a and 20b and show a smooth, nanograined films, consistent with the AFM data in Figure 17, only showing scratches from the stainless steel disc substrate. After cycling at 1C for 100 cycles the films were imaged again at the same magnifications as seen in Figure 21c and 21d. The films are no longer smooth but consist of large porous structures, where the stainless steel disc is clearly visible below, and have gained a "fuzzy" structure.

To better quantify the observed degradation of the ALD RuO_2 electrochemical impedance spectroscopy (EIS) was done at three different stages - after fabrication of the coin cell (un-cycled), after the first discharge/charge cycle, and after the 100th cycle, where the latter two were evaluated by EIS at a 1C rate. The inset of Figure 7 shows the equivalent circuit used to interpret this data, where R_Ω refers to the Ohmic resistance of the cell including the electrolyte, C_{dl} is the capacitance due to the double layer, R_{ct} is the charge-transfer resistance, and W is the Warburg impedance [107].

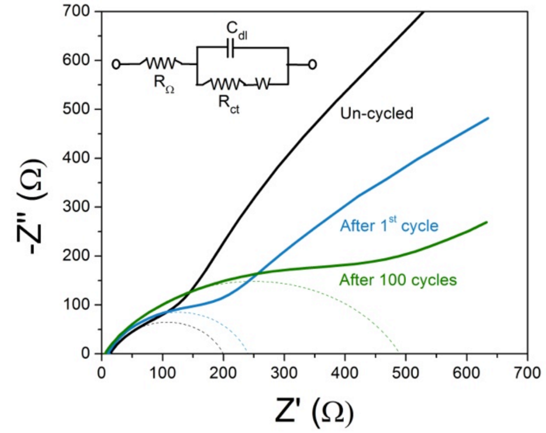

Figure 22. Electrochemical impedance spectroscopy of RuO_2 ALD films. (inset) Shows the model used to interpret the results. The enlarging semi-circles show an increase in resistance from ~200 Ω to ~250 Ω after the first cycle, and ~500 Ω after 100 cycles. Showing an increase in resistance at the RuO_2/electrolyte interface most likely due to SEI formation.

The enlarging semicircles seen in Figure 7 indicate an increase of charge transfer resistance at the RuO_2/electrolyte interface from ~200 Ω to ~250 Ω after the first cycle, and ~500 Ω after 100 cycles. Since the half-cells are discharged to such low voltages, electrolyte breakdown and SEI formation are inevitable and are the standard explanation for this behavior, though the large structural changes may also significantly contribute.

3.5 Conclusions

The high initial capacity of RuO_2, expected from its theoretical capacity, makes it attractive for electrochemical storage, though this is significantly compromised by its capacity degradation as seen at higher rates or due to cycling. The prominent structural changes observed by SEM suggest degradation mechanisms linked to structural change, one of the many fundamental mechanisms that control capacity degradation, all of which remain a pervasive challenge in electrochemical storage across a wide range of materials. Despite this degradation the ability to synthesize high capacity RuO_2 by ALD is promising in two senses. First, ALD is uniquely capable of the high conformality and deposition control needed for fabrication of heterogeneous nanostructures, e.g. incorporating current collector, active storage material, and passivation (or artificial SEI) layers. By making such structures it may be possible to subvert some of these mechanism and significant amount of work using ALD, mentioned in Chapter 1.2, has begun to ask and answer this question. Second, such heterogeneous nanostructures open new possibilities for robust electrode designs (e.g. nanowires) less susceptible to degradation at high rates and upon cycling [108]. Together these factors argue in favor of applying ALD RuO_2 (and other ALD materials) to nanostructured electrodes to better understand degradation mechanisms and to achieve significantly better capacity retention.

It is also important to note that while physical degradation mechanisms were seen, and may explain some of the loss in capacity, key properties of RuO_2, namely its claimed nearly perfect efficiency, are called into question from these results [39]. The completion of this work leads to the work presented in Chapter 4 that aimed to answer that question specifically, what causes the large and fast degradation of this material.

Chapter 4: Lithiation/Delithiation of Single Crystal RuO_2 Nanowires: An In-Situ TEM Study

4.1 Motivation and Introduction

A few simultaneous events led to this work. First, as mentioned, on January 16th 2012 a fire destroyed most of the equipment in our lab, which, after the first few weeks of clean up, left little to do while new equipment orders were written and deliveries were waited for. A relatively new collaboration between Sandia National Labs and University of Maryland had also begun. Exciting work using in-situ TEM techniques offered a unique chance to answer some of the questions the results in Chapter 3 had offered. Therefore it was decided significant effort could be put into what was once a side-project while the lab was repaired from the fire, the results of which would be important for this dissertation.

4.1.1 In-Situ TEM for Battery Materials

A variety of battery materials have been studied using several different configurations inside the TEM. Three different electrolytes including an ionic liquid electrolyte (ILE), a solid Li_2O electrolyte, and ALD coated LiAlSiO have been used [109, 110]. Anode materials such as SnO_2 [111-115], Si [116-121], Ge[122], carbonaceous materials such as multi-walled carbon nanotubes (MWCNT) and graphene[123, 124], oxides such as ZnO [125], a variety of coated materials such as a-Si on MWCNT and carbon fibers [126, 127], Si nanoparticles in a carbon matrix[128], and even a full single nanowire battery with a solid state electrolyte [129] have all been studied using this technique. These results showed that each material behaves differently during the lithiation/delithiation process although some general trends were observed including, large amounts of stress at the lithiation front, usually observed by a dense area of dislocations, volume expansions during lithiation, and often embrittlement of the nanostructure while lithiated [109, 110].

Very little work has been done with this technique characterize conversion reaction Li-ion battery materials. A short study was published on CuO [130] NWs and showed that the reaction mechanism converted to Cu and Li_2O similar to proposed reaction mechanism for RuO_2.

The theoretical capacity of 1410 mAh/g is nearly 4X greater than standard carbon based anodes, however the rapid degradation prevents practical usage. From the literature discussed in Chapter 3 we have seen that the reaction proceeds as follows $RuO_2+4e^-+4Li^+\leftrightarrow Ru^0+2Li_2O$, however the same reports used ex-situ TEM analysis to show intermediate phases, $Li_{0.86}RuO_2$ and $Li_{1.2}RuO_2$, that were also seen in Figure 20(a) for the RuO_2 ALD films [39]. The combination of the results shown in Chapter 3 and what has been reported in the literature do not explain the rapid degradation seen in the cycling data shown in Figure 20(b). This chapter aims at understanding degradation of the RuO_2 through the use of in-situ TEM.

4.2 Experimental Equipment and Procedures

4.2.1 Single Crystal RuO_2 Nanowire Growth

RuO_2 nanowires were grown using vapor transport methods available in the literature [131-134]. Silicon wafers were coated with a 2 nm layer of gold and cut into roughly 1 cm by 1cm pieces. The Au acted as the catalyst for nanowire growth. In a commercially available Atomate Nanowire Growth System, which contains a three-zone furnace, a boat of RuO_2 powder (99.99% Aldrich) was placed at one end of the furnace and the Au coated Si wafers placed downstream of the eventual gas flow at the far end, each in separate zones. The system was then pumped down to 2 torr and purged with 100 sccm of Ar (99.99%, Praxair) for 5m. The RuO_2 powder and Au coated Si substrates were then ramped 950°C and 670°C respectively. Once the temperature was stabilized O_2 (99.99%, Praxair) was flowed at 200 sccm for 10h. The pressure was maintained at 2 torr throughout the reaction. After growth the RuO_2

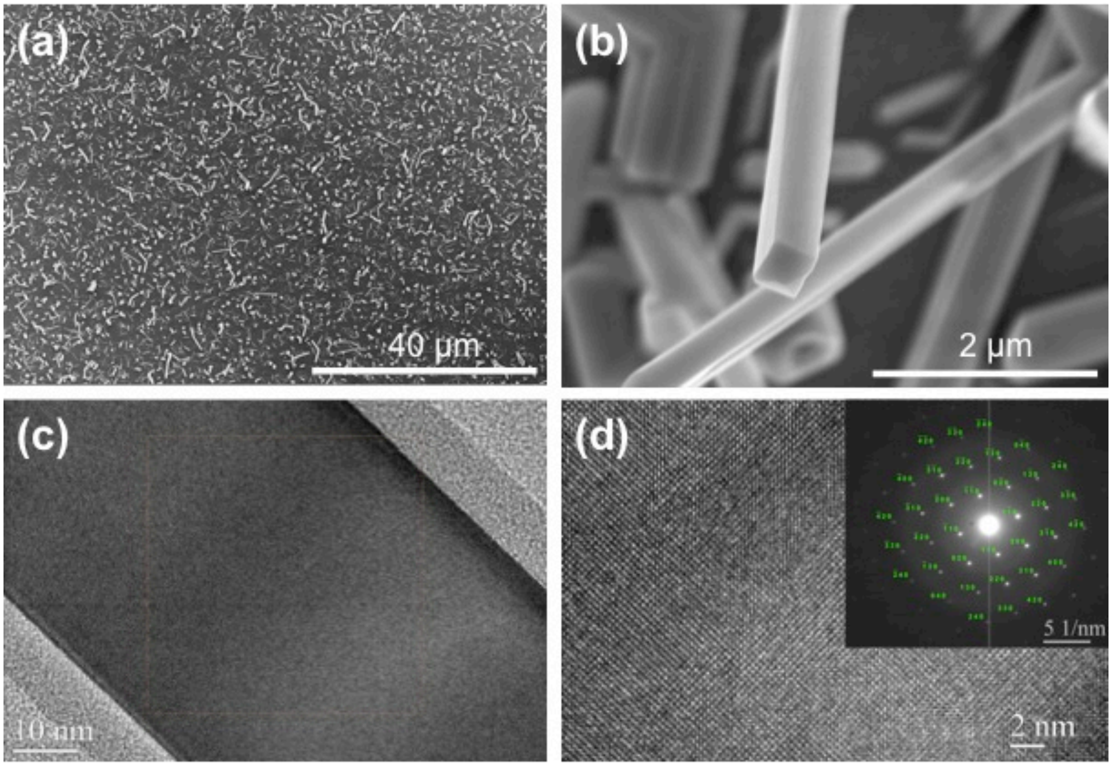

Figure 23. Characterization of the as grown RuO_2 nanowires. (a) shows a SEM image of a large array with (b) showing a higher magnification of the same nanowires. TEM images (c-d) were also taken confirming that the wires are single crystal and rutile (in set (d)).

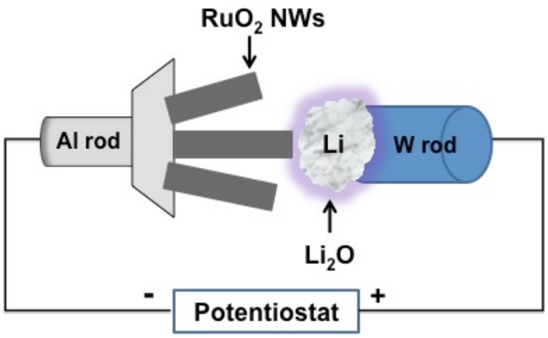

Figure 24. Schematic of the in-situ TEM setup showing.

nanowires were characterized using a Hitachi SU-70 SEM and a Joel 2100F TEM.

The results of this growth process are shown in Figure 23(a-d). Large arrays of nanowires of mixed diameter and length can be seen in Figure 23(a). The majority of the nanowires have diameters between 30 and 90 nm and the lengths vary from 1 to several microns, though it should be noted that larger particles were also present and can be seen in Figure 23(b). These results compare well to the few reported growth recipes in the literature [132-134]. TEM images show that the nanowires are single crystal rutile structure as can been seen in Figure 23(d), Figure 23 (c), and the corresponding inset.

4.2.2 In-Situ TEM

The in-situ experiments were conducted in a FEI Tecanai F30 TEM. A schematic of the experimental setup is shown in Figure 24. Li metal was scratched off a newly cut surface of bulk Li with a tungsten (W) rod in a helium filled glove box (H_2O and O_2 concentrations below 1ppm) and served as the counter electrode and Li source. An aluminum rod was dragged across the surface where the RuO_2 nanowires were grown and held in place by Van der Waals forces. The two electrodes were then mounted onto a Nanfactory TEM-scanning tunneling microscope (STM) holder, which was placed into a plastic bag and sealed in the dry helium environment. During the loading process the Li was briefly exposed, 2~5s, to air forming a native Li_2O layer which served as a solid-state electrolyte. Li_2O makes a good electrolyte for these applications due to its large band gap of ~8eV, a low potential barrier for Li^+ conduction of 0.4 eV, and diffusivity of Li^+ on the order of 10^{-10} cm^2 s^{-1} [109]. Once the samples were loaded into the TEM contact was made between the RuO_2 NW and Li_2O and a potential was applied.

4.2 1st Cycle Lithiation of a Single Crystal RuO_2 Nanowire

In order to lithiate the nanowires a -2V potential was applied, Figure 25(a-d) shows the lithiation of a RuO_2 nanowire, as well, as the electron diffraction patterns (EDP) before and after, Figure 25 (e-f), the reaction front Figure 25(h), and a high-resolution image after the reaction has completed, Figure 25(i). A ~41% increase in the diameter and ~1% increase in the length is seen for the first cycle of lithiation, for a total volume expansion of ~95%. As the nanowire lithiates it becomes a poly crystalline mixture of metal-Ru and Li_2O as apparent from contrast change in the bright field images, Figure 25(a and d), and the EDPs which shows the single crystal rutile structure in Figure 25(e) and the diffraction rings in Figure 25(f) changing from single crystal RuO_2 to the poly crystalline mixture. Indexing the EDPs confirms the rutile structure for the nanowire showing a growth direction of [010]. After lithiation the {111}, {220}, and {311} Li_2O planes become visible, as well as the Ru {111} and {200} planes.

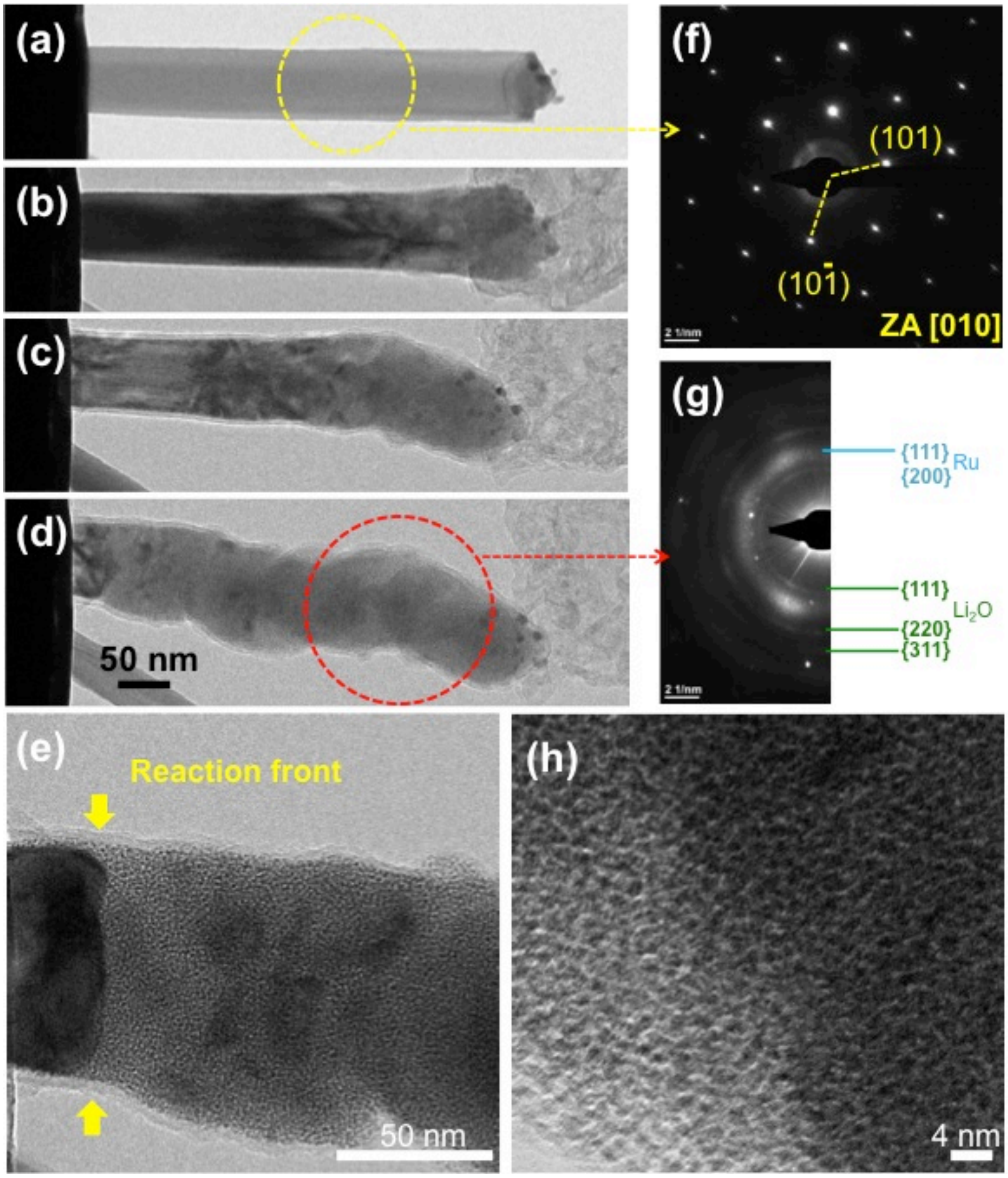

Figure 25. Lithiation of a single crystal RuO_2 nanowire. (a-d) show the propagation of the reaction from RuO_2 to a matrix of Ru and Li_2O. Confirmation of the presence of these two phases is seen in the before and after EDPs in (f) and (g). The cloud of dislocations indicative of the reaction front is shown in (h) and the fully lithiated nanowire is shown in (i)

At the reaction front, as seen in Figure 25(h), a large cloud of dislocations is visible similar to those seen for SnO_2 nanowires corresponding to an area of high stress [111]. On either side of the dislocation cloud it can be seen that the single crystal nanowire is still pristine or fully reacted becoming a network of Ru and Li_2O,

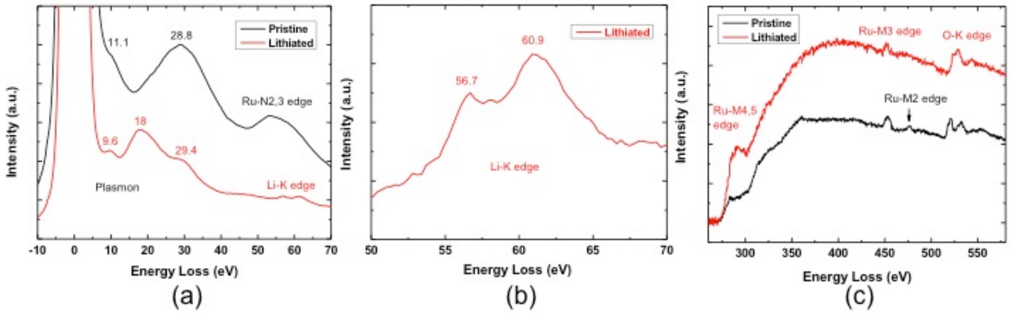

Figure 26. Electron energy loss spectroscopy before and after lithiation. (a) shows low loss region where the disappearance of the Ru $N_{2,3}$ edge and the emergence of Li-K edge after lithiation are seen. A more detailed view of the Li-K edge seen in (a) is shown in (b) confirming the presence of Li. The core loss spectrum in (c) shows a decrease in the Ru-$M_{3,2}$ edge while the Ru-$M_{4,5}$ edge increased during lithiation.

seen in greater detail in Figure 25(i) as the reaction reaches completion. As compared to previous reports[39, 40] we could not confirm the presence of individual nanoparticles of Ru in a matrix of Li_2O, but rather, it appears to be a network Ru and Li_2O, which explains the reversibility of the reaction. These conclusions are discussed in greater detail in Chapter 4.4. To confirm the presence of Ru and Li_2O electron energy loss spectroscopy (EELS) was conducted while the nanowire was fully lithiated and in pristine condition. The results are shown in Figure 26(a-c).

The low loss EELS spectrum in Figure 26(a) shows the Ru $N_{2,3}$ edge that, upon lithiation, disappears showing the Li-K edge which can be seen in greater detail in Figure 26 (b).The Li-K edge appears to be similar to the spectrum expected of Li_2O rather than metallic Li[135]. The core loss spectrum can be seen in Figure 26(d). After lithiation the Ru-$M_{4,5}$ edge increased while the Ru-$M_{3,2}$ edge decreased [136, 137]. From these results it can be concluded that fully lithiated RuO_2 nanowires consist of metallic Ru and Li_2O.

In order to observe the intermediate phases the potential was slowly increased from 0 to -1V and series of EDPs were taken during lithiation with the results shown in Figure 27. The EDP of a pristine single crystal RuO_2 nanowire can be seen in

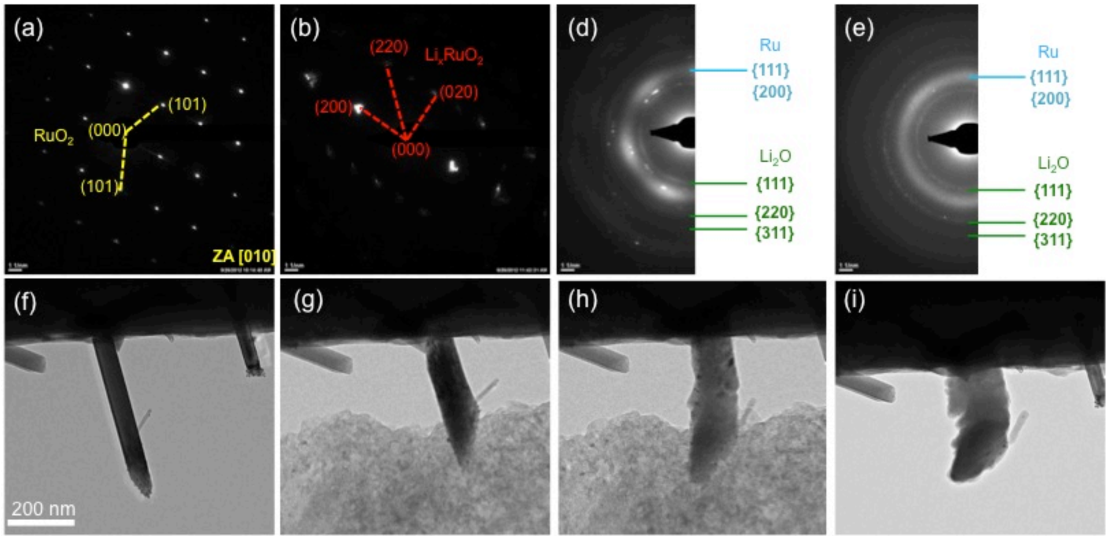

Figure 27. A series of EDP and bright field images confirming the presence of the intermediate phase Li$_x$RuO$_2$, where x is close to 1.

Figure 27(a), as well as its bright field image in Figure 27(f). When the nanowire was put into contact with the Li$_2$O and a potential was slowly increased lithiation began. Figure 27(b) shows the EDP of the intermediate phase Li$_x$RuO$_2$, where x is close to 1, which is an orthogonal crystal structure. Because the reaction happened so fast it was difficult to observe the specific x=0.86 and x=1.2 phases reported using ex-situ TEM analysis in the literature. It can also be seen by comparing the EDP in Figure 27(b) to the bright field image in Figure 27(g) that a large cloud of dislocations was present, indicating that this is a high stress, most likely unstable phase. Continued lithiation shows the transition from the intermediate phase to the final products Ru and Li$_2$O, as shown in Figure 27(d), showing that all three phases exist at the same time. Again a comparison can be made to the bright field image, Figure 27(h), showing dissipation of the dislocation cloud. Finally the fully lithiated nanowire EDP can be seen in Figure 27(e) and its corresponding bright field image in Figure 27(i). The fully lithiated EDP only shows the presence of the Ru {111} and {200} planes and the Li$_2$O {111}, {220}, and {311} planes as seen in Figure 26(g).

4.2.1 1st Cycle Lithiation Conclusions

From the results shown in Figures 25-27 we can conclude that the lithiation of a single crystal nanowire does not proceed as was reported in the literature but rather passes through a high-stress intermediate phase first. Continued lithiation brings upon a second phase change where the only two species present are metallic Ru and Li_2O. However to gain a full understanding of material as it relates to Li-ion storage multiple cycles would have to be conducted, which is covered in the next section.

4.3 Multiple Cycling

Figure 28(a-n) shows a single RuO_2 lithiated and delithiated three times. To lithiate the nanowire a -2V potential was applied, delithiation was achieved by applying a +4V potential. Again a pristine single crystal nanowire was chosen as can be seen Figure 28(a) and Figure 28(h). The nanowire volume expansion is again seen to be ~95% after lithiation and is, as expected, again composed of Ru and Li_2O, seen in Figure 28(b) and (i). After the first delithiation however, ~26% of this volume expansion is irreversible and the nanowire becomes amorphous RuO_2 (a-RuO_2) as can be seen from the contrast changes between Figure 28(a) and Figure 28(c), and more dramatically in the comparisons of the EDPs seen in Figure 28(a) and Figure 28(j). Where the rutile diffraction pattern is easily identifiable for the pristine RuO_2 wire after delithiation all that remains is an amorphous halo. After the first delithiation the reaction mechanism proceeds between a-RuO_2 and a network of polycrystalline Ru and Li_2O as can be seen in the EDPs shown in Figure 28(i-f). The intermediate phase was no longer visible after the first cycle.

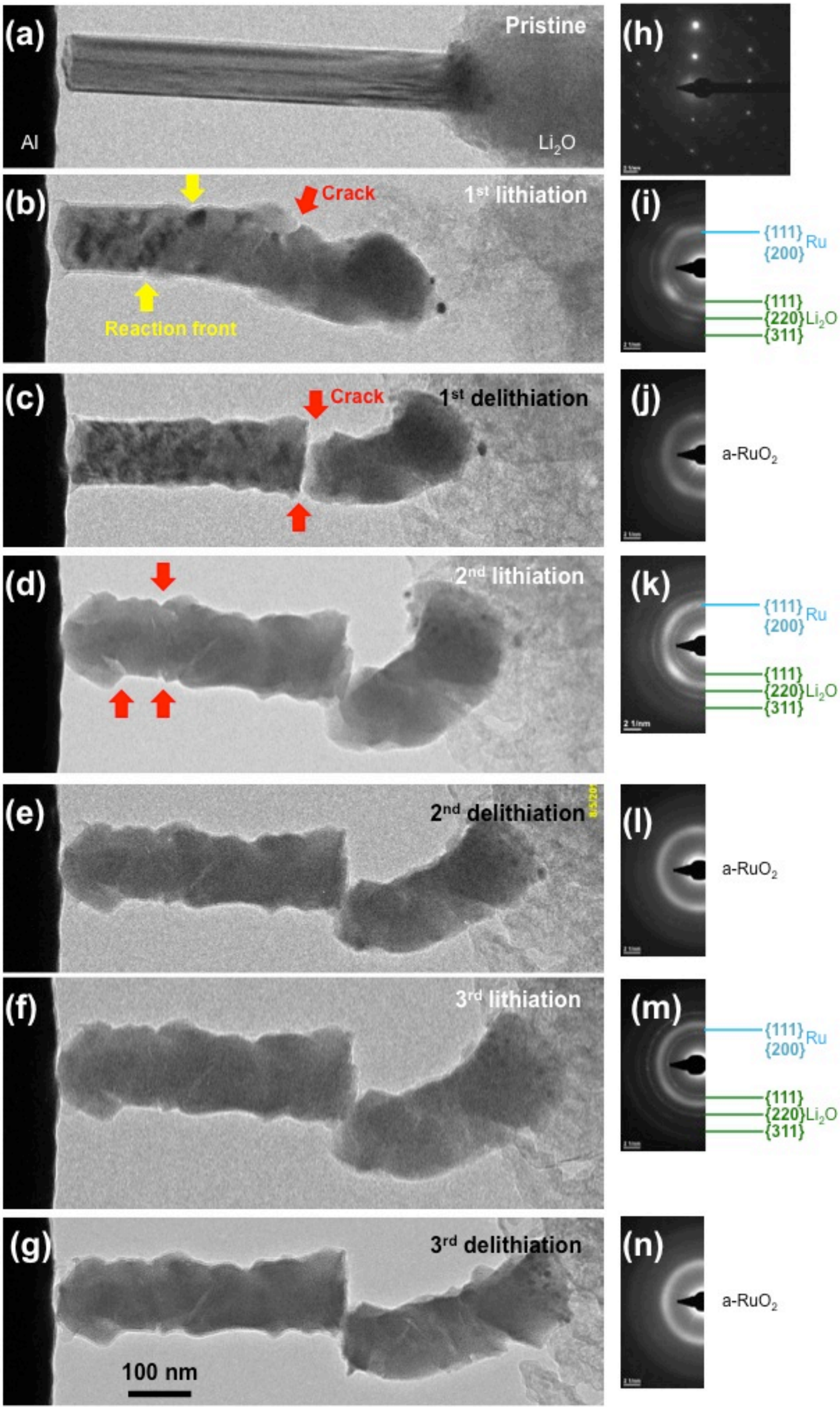

Figure 28. Multiple cycling of a single RuO_2 nanowire.

During the cycling process mechanical degradation also becomes apparent as the surface of the nanowires is seen to become rough, Figure 28(b-g), and cracks begin to appear, Figure 28(b-d), due to lithium embrittlement, a phenomenon seen for several other materials during in-situ TEM experiments [109, 110]. Despite crack formation electronic an ionic conductivity remain high and the entire structure can be lithiated and delithiated for all three cycles. All nanowires tested exhibited cracking during the cycling process.

To determine if the reaction was fully reversible high-angle annular dark-field scanning transmission electron microscopy (HAADF-STEM), Figure 29(a), and HRTEM, Figure 29(b) were taken after the 3rd delithiation. It is apparent from these images that the reaction is not fully reversible with some areas still contain networked Ru and Li_2O rather than a-RuO_2. From these data and the data shown in Figures 25-28 we can give a full picture of the reaction mechanism, the degradation effects, both chemical and mechanical, and their effects on the capacity of the material.

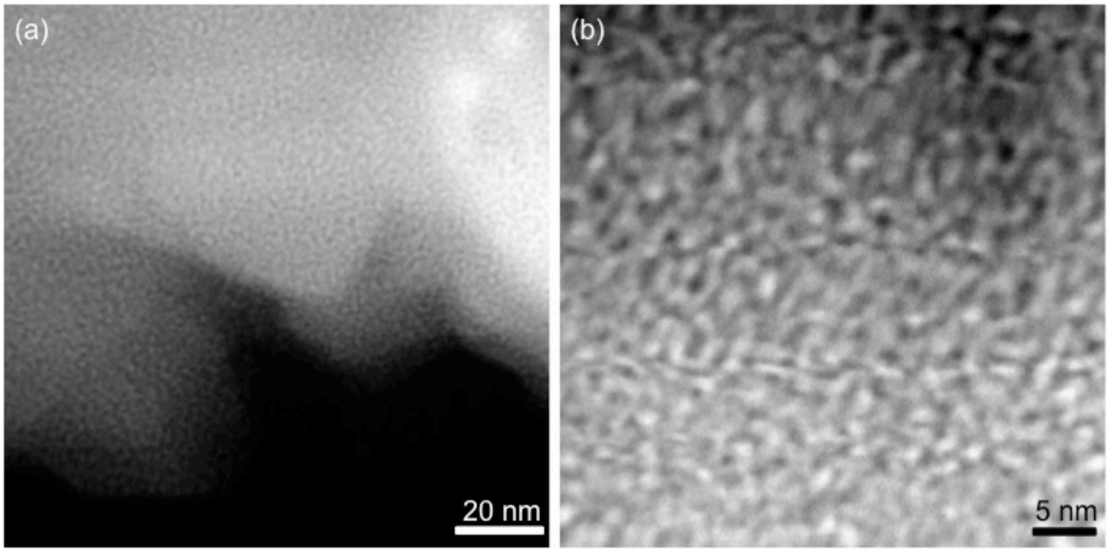

Figure 29. HAADF-STM (a) and HRTEM images of an RuO_2 nanowire after the 3rd delithiation showing residual Ru and Li_2O.

4.4 Conclusions

The published reaction mechanism $RuO_2+4e^-+4Li^+ \leftrightarrow Ru^0+2Li_2O$ does not give the full picture of what happens during the cycling of RuO_2. From the data shown in Figure 25 we can confirm that the 1st lithiation step proceeds as follows;

$$RuO_2(c)+xe^-+xLi^+ \rightarrow Li_xRuO_2(c)$$

Upon continued lithiation the reaction then proceeds;

$$Li_xRuO_2(c)+(4-x)e^-+(4-x)Li^+ \rightarrow Ru^0(c)+2Li_2O(c)$$

The reaction only becomes reversible after the first cycle and proceeds as follows;

$$RuO_2(a)+xe^-+xLi^+ \leftrightarrow Ru^0(c)+2Li_2O(c).$$

The reversibility is further hampered by mechanical degradation seen in the form of crack formation and surface roughening in Figure 28 as well as chemical irreversibility seen in Figure 29. The chemical irreversibility is most likely due to the nanostructured network of Ru and Li_2O formed while lithiated. The network of Ru allows a highly conductive pathway for electron transport while the Li_2O provides the same pathway for Li^+, thus allowing the reaction to be reversible. Since the network formation is seemingly random it is possible that some part of the structure become electronically or ionically disconnected from the rest of the structure, therefore making it impossible to reverse the reaction for that section of the material. At each cycle some small part of the nanowire is no longer active, overtime this could significantly reduce the capacity, as seen in the ALD films in Chapter 3.

The implications of these results are two fold. In terms of the work presented using the ALD films it is clear that degradation seen in the thin films has both a mechanical and chemical part and, as with many materials with promising high capacities, such as Si, Ge, and Sn, nanostructuring may be able to offer ways to defeat these limitations, as has been seen for the same materials mentioned [138, 139]. With ALD capable of creating incredibly thin layers over high-aspect-ration structures, the focus of Chapter 5, it will be shown that nanoengineering this material does offer improvements.

Secondly, further insight into the behavior of other conversion type materials may also be gathered from these results. Less expensive materials such as, FeS_2, MnO_2, and TiF_3, may behave in similar ways [103]. It may be possible to choose a material such that the reaction by-products are not electrically insulating Li_2O, but rather a conductive nitride or phosphide material for example, thus eliminating the chemical irreversibility.

Chapter 5: Fabrication and Characterization of 3D RuO_2 Batteries

5.1 Introduction

As mentioned in the conclusion of the previous chapter there is a variety of materials with specific capacities higher than carbon, which remains the standard in Li-ion batteries. Most of these materials, including RuO_2, cannot compare to the cyclability of carbon due to a variety of degradation mechanisms. A popular example is that of Si, which boasts the impressive theoretical capacity of 3,579 mAh/g, but has been shown to pulverize upon repeated lithiation preventing practical implementation [108]. By nanostructuring this material, i.e. making/growing nanoparticles and/or nanowires, significant improvement on the cycling stability over the bulk has been shown [138].

In Chapter 1.3 it was noted that ALD has recently been shown to improve a variety of different battery metrics by either coating with a passive material in an attempt to prevent degradation or directly depositing active materials over high-aspect-ratio structures. This chapter explores the later approach in an attempt to improve the cycling stability of RuO_2. With the degradation mechanisms revealed in Chapter 4 in mind we used the ALD process developed in Chapter 2 to make high-aspect-ratio nanostructures in an attempt to improve the battery performance studied in planar form in Chapter 3.

During the proposal of this project four possible configurations of nanostructures, all made through a template method, were chosen as shown in Figure 30. These structures can be divided into two categories nanotubes, shown in Figure 30(a) and Figure 30(b), and nanowires, shown in Figure 30(c) and Figure 30(d). Besides their geometry the proposed structures vary in two other ways. The charge collection material either TiN or Ru, and the TiO_2 layer required to nucleate the Ru, as discussed in Chapter 2. It was decided to eliminate structures using Ru for two reasons. First the fact that Ru is one of the reaction products after lithiation of RuO_2 could lead to slow consumption of this layer during cycling. Secondly the addition of the TiO_2 nucleation layer is not desirable as it further constrains an already severally constrained geometric space and adds additional weight. This leaves the TiN charge collection layer nanopore and nanowire based geometries. The nanopore geometry was eliminated because of concerns for electrolyte access. It was decided that more theoretical modeling needs to be done on systems like this, particularly addressing Li^+ concentrations inside such severally constrained geometries. Therefore the template based 3D structure that will be discussed in this chapter is shown in Figure 30(c). For comparison to these structures multi-walled carbon nanotube (MWCNT) sponges were also used to fabricate 3D electrodes and are discussed in Chapter 5.4.

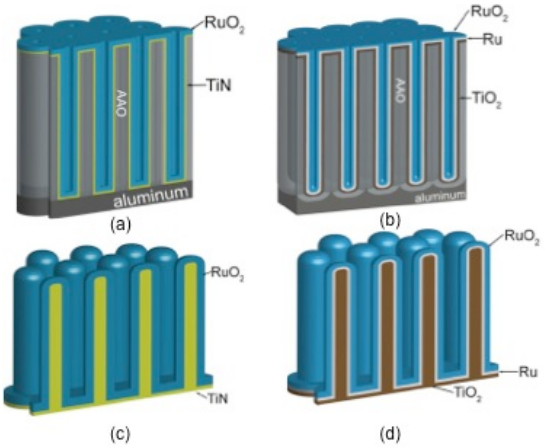

Figure 30. Schematic of the proposed nanostructures to be fabricated through porous anodic alumina and ALD.

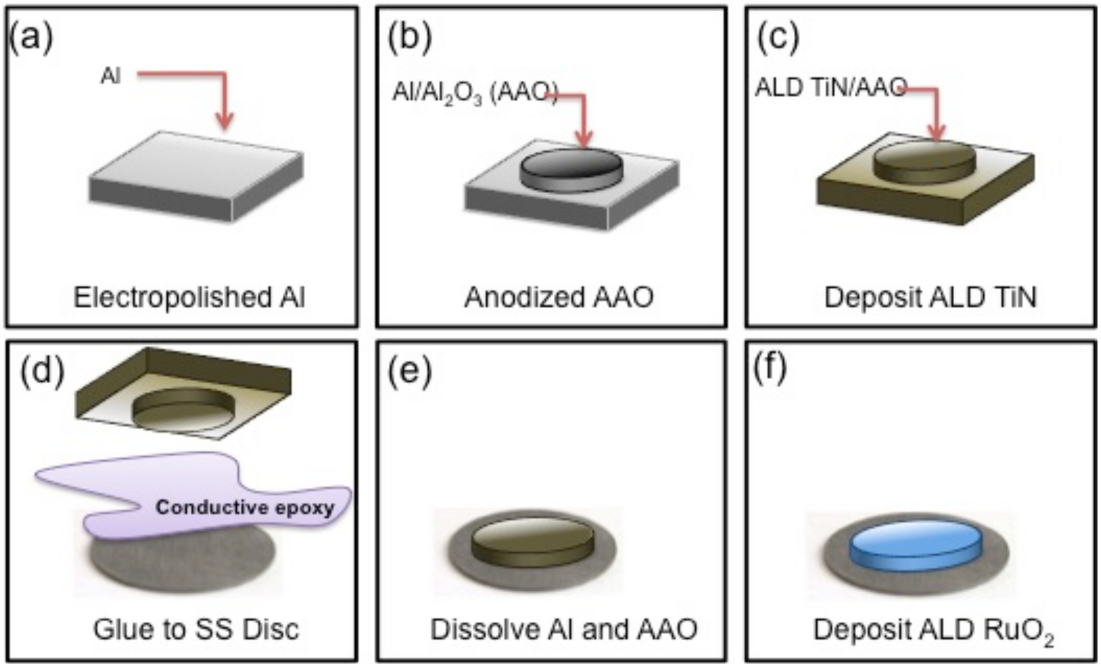

Figure 31. A schematic of the fabrication of TiN/RuO_2 core/shell nanowire arrays. The process starts with a piece of electropolished Al (a) that is then masked and anodized (b). Next the pores are filled with ALD TiN (c) and attached to a stainless steel disc (d). The Al is then dissolved followed by the template leaving an array of TiN nanowires (e). Finally the nanowires are coated with RuO_2 using the process described in Chapter 2.

5.2 Fabrication of Large Arrays of TiN/RuO_2 Core/ShellNanowire Electrodes

The fabrication of the TiN/RuO_2 core/shell nanowire arrays is depicted in Figure 31 (a-f) and discussed in detail below.

5.2.1 Growth of Porous Anodic Aluminum Oxide (AAO)

Sheets of pure aluminum (99.999%) are degreased in acetone by sonication for 10 minutes. The samples are then electropolished in a 5:1 mixture of ethanol and perchloric acid ($HClO_4$) for 5 min at 3°C. After the samples have been polished a two-step anodization process is done where first a larger sheet (generally 2 in. x 1 in.) is anodized in a 0.3M oxalic acid ($H_2C_2O_4$) solution below 10°C for 6h producing an array of disordered alumina nanopores. These nanopores are then removed by dissolution in a 70% phosphoric acid (H_3PO_4), 30% chromic acid (H_2CrO_4) solution at 60°C overnight. Next the samples were cut into roughly 2 cm x 2 cm squares, put into a holder with a 1.27 cm (0.5 in) diameter aperture and anodized a second time in 0.3M oxalic acid ($H_2C_2O_4$) again below10°C. The growth rate of the nanotubes is 70nm/min. The as-grown AAO pores have a diameter of ~30 nm that were then widened to ~50 nm in a 1:1 solution of ammonium hydroxide (NH_4OH) in H_2O. Further details about the two-step anodization process can be found in the following references [140-142].

5.1.2 Fabrication of TiN/RuO_2 Nanowires

The pore-widened templates are then baked overnight to remove any residual water and were placed into a Cambridge Nanotech Fiji where 500 cycles, ~25 nm of TiN was deposited using the standard precursors tetrakis dimethylamino titanium and ammonia, completely filling the pores. The templates were then flipped over and glued to a stainless steel disc using Duralco 124 (Cotronics) chemical resistant high temperature silver based epoxy, which was annealed for 4hrs at 125°C, followed by a post-anneal at 175°C, a schematic of this is shown in Figure 31(d).

Next the Al and AAO are removed. A 1M copper chloride ($CuCl_2$) in hydrochloric acid (HCl) solution was used to dissolve the Al, which leaves behind a small amount of Cu. To remove the residual Cu the samples were briefly dipped into a 1:1 Nitric Acid (HNO_3) in H_2O. Finally the AAO template was dissolved in a 3M sodium hydroxide (NaOH) solution for 40mins, leaving behind an array of TiN nanowires perpendicular to the stainless steel disc, as shown in Figure 31(e). In order to prevent the nanowires from sticking together they were washed for 5m in the following order, descending in polarity, H_2O, acetone, ethyl acetate, and finally

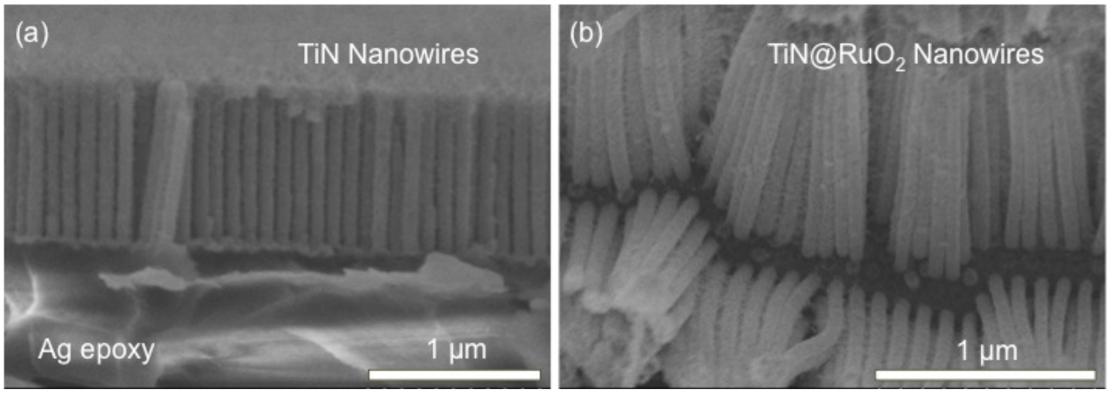

Figure 32. SEM images showing the 1μm nanowire arrays before (a) and after (b)

hexanes. Next 660 cycles of RuO_2, was deposited by ALD as described in Chapter 2. The samples were weighed both before and after the RuO_2 deposition. Figure 32 shows SEM images of the completed process. Despite using the above mentioned wash sequence samples with nanowires longer than ~1 μm did stick together in some areas. To confirm that the ALD coating was conformal TEM analysis and EDS line scans were also done and are shown in Figure 32(a) and Figure 32(b). These data show two pieces of broken nanowires with the Ru peaks stronger at the edges and the Ti peaks stronger at the centers, thus confirming the desired core/shell structure.

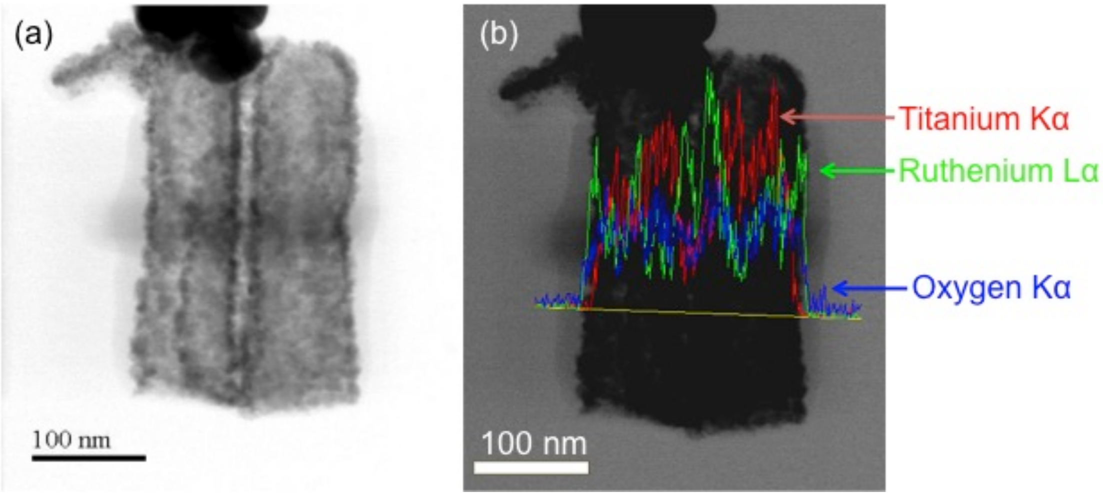

Figure 33. STEM image (a) and EDS spectra (b) of the RuO_2 coated TiN nanowires. These data confirm the core-shell nature of the nanowires.

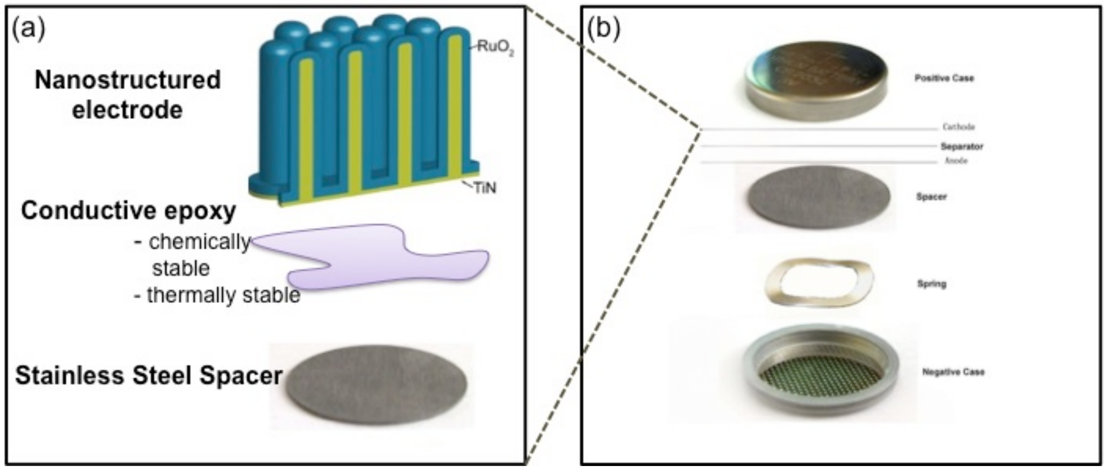

Figure 34. Schematic showing a summary of the nanowire electrode fabrication and the integration into coin cells.

5.1.3 Integration Into Coin Cells

By using the stainless steel discs, integration into coin cells was simple. Fabrication was accomplished exactly as described in Chapter 3.2 with additional steps described in the previous section on fabricating the nanowires, as shown by the schematic in Figure 33.

5.3 Electrochemical Characterization of TiN/RuO$_2$ Nanowires

The first cycle discharge curves for four sets of nanowires and a planar control sample are shown in Figure 34(a). As with the planar studies shown in Chapter 3.3 the nanowire batteries were cycled between 4.3V and 0.05V. An increase in the areal capacity is seen as a function of nanowire length. The planar control films showed a capacity of only ~75 μAh/cm^2, while the 500 nm nanowires showed an increase in capacity with a value of ~275 μAh/cm^2. Further increasing the nanowire length showed an increase in areal capacity with values of ~350 μAh/cm^2 for 1 μm, ~400 μAh/cm^2 for 5 μm, and ~475 μAh/cm^2 for the 10 μm nanowires. These results are

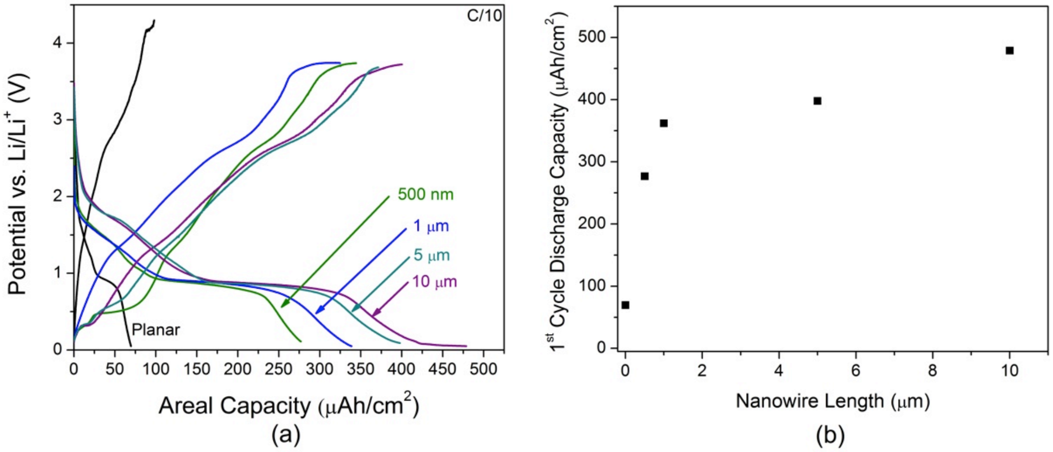

Figure 35. Electrochemical characterization of TiN/RuO$_2$ showing in increase in the areal capacity as a function of nanowire length (a). The results of this data are summarized in (b) which shows the 1st cycle discharge capacity as a function of nanowire length.

summarized in Figure 34 (b), which shows the first cycle discharge capacity as a function nanowire length. These data show saturation like curve rather than the expected linear increase. A variety of reasons may explain this data including, not quite conformal coating of the longer nanowires either due to the processes it self, or the longer nanowires sticking together after the template has been removed. Furthermore, it should also be noted that none of TiN/RuO$_2$ batteries tested survived past the first cycle. Because of this further investigation was stopped.

5.3.1 Possible Failure Mechanisms

Figure 36 shows TEM images of the TiN/RuO$_2$ nanowires after the first cycle. The RuO$_2$ coating is adhering well to the TiN charge collection layer though it does appear the volume has expanded as compared to the results shown in Figure 33. Therefore we conclude that the failure after the first cycle is not due to an intrinsic material failure, i.e. some interaction between the TiN, RuO$_2$, or other battery components.

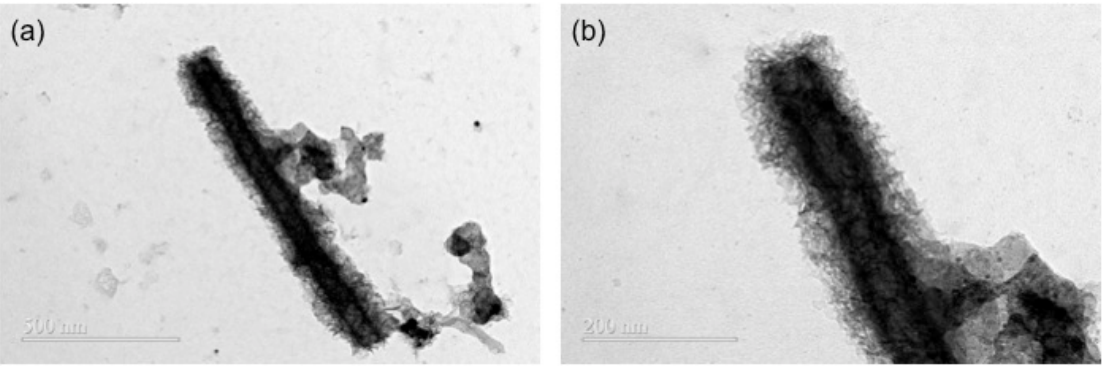

Figure 36. TEM images of TiN/RuO_2 nanowires after the first cycle. Images clearly show an intact RuO_2 layer though expanded due to lithiation.

The most likely cause for this failure is the silver in the epoxy. Silver has been shown to begin to lithiate at potentials of 0.35V through an alloying mechanism, similar to Sn and Si [143-145]. Silver continues to lithiate at lower potentials eventually reaching $AgLi_{12}$ at 0.05V, at this potential a volume expansion of 82% has been reported [145]. Because of the low potentials used here and cracks in the TiN/RuO_2 nanowire layer it is most likely the case that the Ag in the epoxy becomes lithiated, expands, and then breaks off as it delithiates. To confirm that the failure is not intrinsic to the material choice but rather extrinsic, i.e. due to the epoxy used to attach the nanowires to the battery electrode, a second 3D structure was fabricated using MWCNT sponges and is described in the following section.

5.4 MWCNT/RuO_2 Nanowire Batteries

5.4.1 Fabrication of MWCNT/RuO_2 Batteries

Carbon nanotube sponges were grown by chemical vapor deposition (CVD) using 1,2-dicyclobenzene as the carbon source and ferrocene as the catalyst. Ferrocene powder was dissolved into 1,2-dicyclobenzene to make a solution with a concentration of 0.06 g/mL. The solution was then injected into a 2 in. quartz tube CVD furnace by a syringe pump at a constant feeding rate of 0.13 mL/min. The

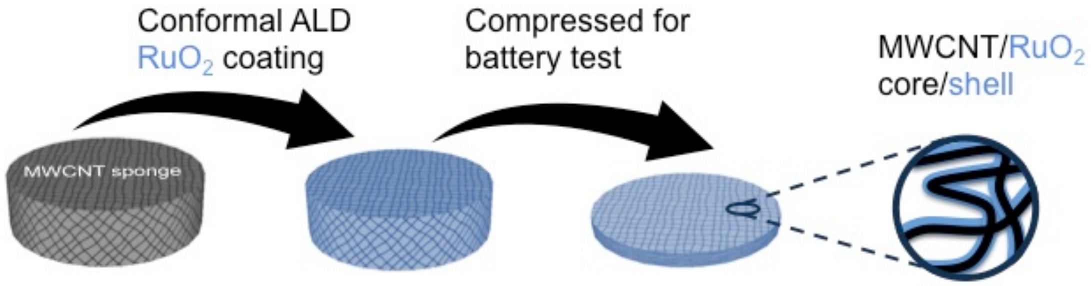

Figure 37. Schematic of the fabrication of MWCNT/RuO_2 battery. ALD allows conformal coating of the highly porous MWCNT sponge taking advantage of the incredibly high surface area. The coated MWCNT sponge is then compressed into a coin cell and tested as a battery.

carrier gas was a mixture of Ar and H_2, at a flow rate of 2000 and 300 mL/min, respectively. Quartz slides were used as the growth substrates that were placed in the center of the furnace at 860°C. Typically the growth time was 4h, which gives bulk sponge samples with thicknesses of about 8-10 mm. Before ALD coating the samples were cut into 1/8 in. diameter, 2mm thick samples. Further information on this process can be found in the following references [28, 146, 147].

A schematic of the process flow can be seen in Figure 37. After the sponges were cut they were weighed, then placed into the ALD reactor where 600 cycles of RuO_2 was deposited. The samples were weighed a second time and fabricated into coin cells using stainless steel discs as substrates, as shown in Figure 18.

TEM images of the coated MWCNT sponges are shown in Figure 38 (a-d). A conformal coating of ~20 nm slightly below (~0.3 Å/cycle) the growth rate reported in Chapter 2 of 0.4 Å/cycle. Growth on MWCNT has been shown to requires defect sites, hydroxyl groups, or carboxyl groups to begin nucleation, the film then grows from that cite coating the tube [148-150]. The results seen in Figure 38(a) and Figure 38(b) are consistent with these previous results. The areas indicated with arrows in Figure 38(b) show areas with no coating, where no cites were available to initiate

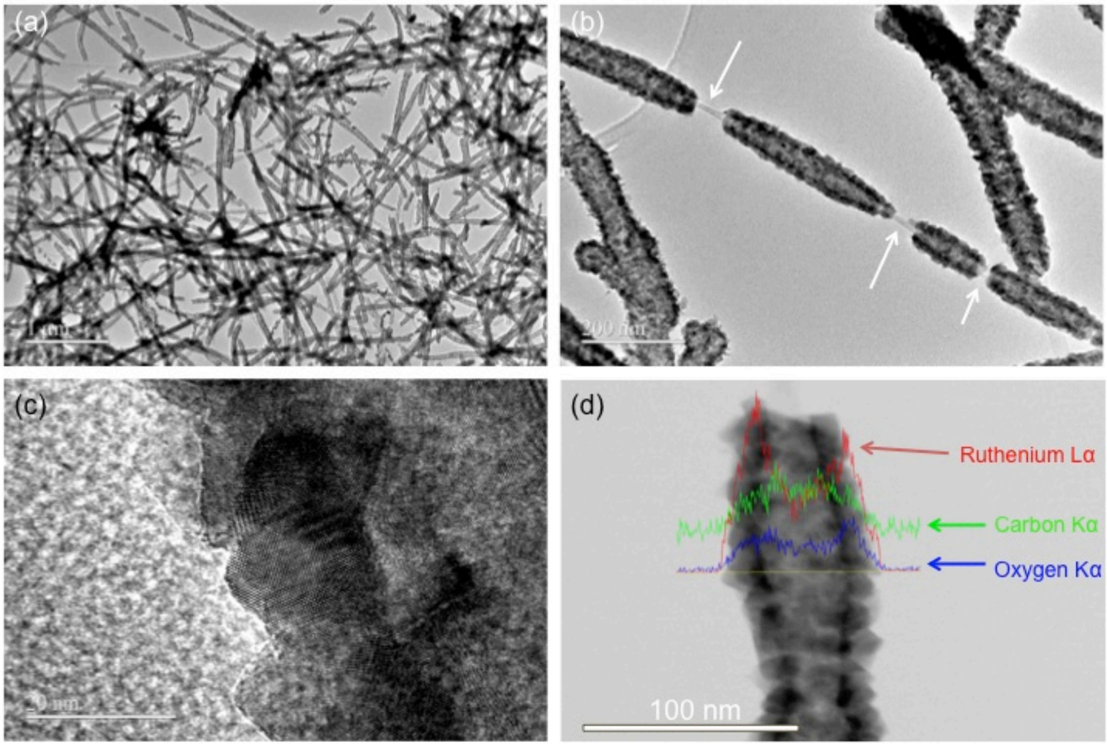

Figure 38. TEM images of MWCNT/RuO$_2$ core/shell nanowires. (a) shows a large number of coated MWCNTs. The arrows in (b) indicate sections of the MWCNT that did not get coated most likely due to lack of nucleation sites. A high-resolution image is shown in (c) confirming the coating is polycrystalline. An EDS line scan is shown in (d) confirming the core shell structure.

growth, increasing the number of deposition cycles or functionalizing the MWCNTs most likely prevent these bare areas. Figure 39(c) shows a high-resolution image of the coating where polycrystalline grains can be seen, consistent with the XRD results reported in Figure 15. The core/shell structure is confirmed in Figure 38(c) using line scan EDS showing Ru peaks stronger on the edges and C peaks strongest in the center, comparable to results shown for the TiN/RuO$_2$ structures discussed in Chapter 5.3.

5.4.2 Electrochemical Characterization

Figure 39(a) and Figure 39(b) shows the 1st cycle areal discharge capacity and cycle stability of the MWCNT/RuO$_2$ structures at 1C respectively. The planar control

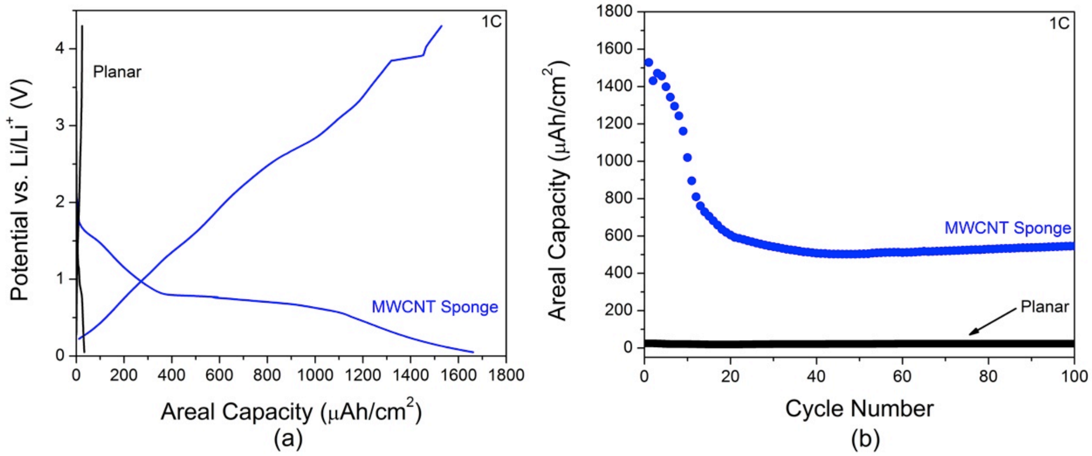

Figure 39. First cycle areal capacity of MWCNT/RuO_2 nanostructure (a) showing ~1600 µAh/cm^2 compared to the planar value of ~30 µAh/cm^2. The cycle stability is shown in (b). The planar capacity drope to ~20 µAh/cm^2 (not visible due to scale) while the MWCNT/RuO_2 nanostructure drops to ~600 µAh/cm^2 after ~20 cycles.

sample showed a ~30 µAh/cm^2 at 1C, while the MWCNT/RuO_2 samples showed a ~50x increase with a value of ~1600 µAh/cm^2. Compared to the TiN/RuO_2 nanostructures, Figure 35(a), this capacity is ~3x than the 10 µm electrodes. However, despite this high first cycle capacity after ~20 cycles the areal capacity drops to a stable value of ~600 µAh/cm^2. TEM analysis was conducted after 100 cycles to compare to compare the morphology of the structures before and after.

Figure 40 is a representative image of the nanowires after 100 cycles. It can be seen that the crystalline structure has disappeared, as expected from the in-situ TEM analysis discussed in Chapter 4, and the surface has roughened. Furthermore, small particles similar to the ones seen in the high-resolution images in Figure 29, which were identified as Ru and Li_2O are present. The results shown here may be the Ru/Li_2O network seen the Chapter 4 data. The data shown in Figure 29 was taken after a single nanowire was only cycled three times, it is conceivable that after 100 cycles a larger amount of larger particles would be present as more of the material becomes inactive. Further investigation of nanowires cycled for longer than three

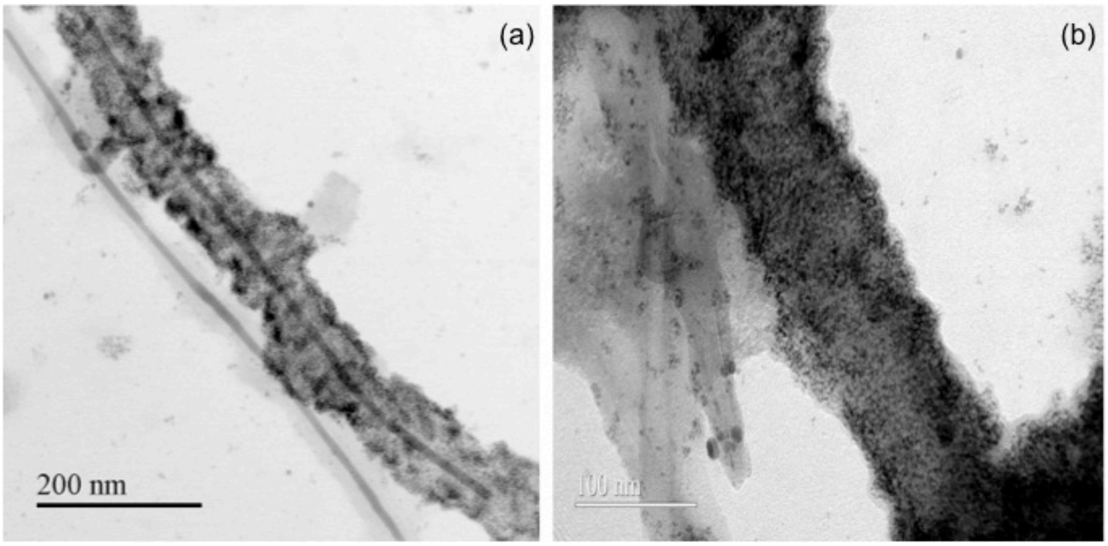

Figure 40. TEM images of the MWCNT/RuO_2 nanostructures after they have been cycled 100 times. Both images show an increased surface roughness, a loss of crystal structure, and the possibility of Ru and Li_2O phases seen in the in-situ TEM data.

cycles, in terms of the in-situ data, or ex-situ, after cycling would be required to get a definitive answer.

5.5 Conclusions

As discussed in the conclusion to Chapter 3, one of the most promising aspects of ALD is its ability to conformally coat high-aspect ratio nanostructures which allows the integration of current collector, active material, and possibly electrolyte all into a single nanostructure or, more practically, an array of nanostructures. The results shown here accomplished this fabrication using two different electrode materials and nanoarchitectures. The TiN/RuO_2 configurations showed that large arrays of heterostructured nanowires could be easily fabricated but were hindered by an in ability to connect electrically from the bulk of the battery to individual nanowires. The epoxy method worked in principle but suffered from the low potentials used to fully lithiate the RuO_2. One could imagine using an active material where the potential can be kept above 0.35V thus preventing lithiation or finding and using an epoxy that does not contain a material which reacts or lithiates at such low potentials.

The MWCNT sponges offer incredibly high surface areas, which combined with ALD, show significant improvement in the areal capacity. Using this architecture the improvement expected from having a thin layer of active material, allowing complete and easy access for the Li^+ to the electron-conducting layer is seen. While the cycle stability does drop after the first ~20 cycles it stabilizes at a reasonable value. Keeping in mind the fundamental irreversibility of the reaction between RuO_2 and Li discussed thoroughly in Chapter 4, these results indicate that using ALD to create mechanically robust heterostructured nanomaterials does offer improvements to materials that would otherwise not be suitable for integration into batteries.

The question remains whether RuO_2 is a good battery material. For scientific purposes yes, it has a high electronic conductivity, a single crystal phase (i.e. rutile), and, thanks to the work presented in Chapter 4, a fully studied reaction pathway. The ability to deposit it through ALD also offers the ability to study it versus more cost effective materials such as MnO_2 or Fe_2O_3. Practically, it is of the author’s opinion that, RuO_2 will never make its way into a commercially available battery; the price of Ru is comparable to, and sometimes more than, the price of Pt, thus making it cost prohibitive. However, should niche applications require this material the ALD process developed here in combination with the electrochemical studies offer a way to deposit only the required amount, in incredibly small quantities, could make such a battery feasible.

Chapter 6: Conclusions and Future Work

6.1 Conclusions

This work achieved four main objectives;

1. Through a collaboration with Air Liquide, a leading precursor provider, a new Ru precursor was developed and successfully shown to deposit Ru, a material of great interest as a contact in the semi-conductor industry. Furthermore, through our knowledge of the energy storage community, due to collaborations with Prof. Sang Bok Lee's group, we exploited the ability to deposit RuO_2 and showed the first fully characterized process parameters for this material. We showed that the difference between the two processes was in controlling the oxygen partial pressure, which effectively changed the amount of subsurface oxygen present during the reaction. By merely changing the flow rates and pulse times of the O_2 exposure step the desired material can be deposited.
2. Using this newly developed RuO_2 process, thin film batteries were fabricated which allowed the first testing of RuO_2 beyond three cycles. These batteries showed an excellent first cycle capacity that quickly degraded. Comparison of these results to those reported in the literature found that very little had been published studying this material. These results led to the next study.
3. Through a collaboration with Sandia National Labs, an in-situ TEM study was under taken to understand the lithiation mechanisms aimed at understanding the rapid degradation seen for RuO_2. These results showed that the

degradation was two fold. First significant surface roughening and mechanical degradation, including cracking, was seen. Second it was shown that the chemical reaction was not completely reversible, therefore each cycle leaves some amount of Ru and Li_2O behind, reducing the total amount of material available for Li^+ storage.

4. Finally, with the degradation mechanism in mind and taking advantage of ALD's extreme conformality, heterostructured nanoelectrodes were fabricated with two different charge collection layers. Despite the failure of the epoxy used to attach TiN/RuO_2 nanowires both this structure and the MWCNT structure showed an increase in areal capacity and, in the case of the MWCNT/RuO_2 structure, showed improved cyclability.

With ALD becoming more prominent in research areas beyond the semi-conductor industry, including energy storage, the work shown here helps to motivate future and continuing work.

6.2 Future Work and Applications

1. As discussed throughout this work ALD's extreme conformality allows the ability to fabricate integrated nanostructures either through all ALD based processes or through the use of other synergistic processes such as ECD and CVD. To this end new processes aimed at fabricating solid-state electrolytes, a variety of active materials, both anode and cathode, and charge collection layers is on going. Work to address the solid-state electrolyte issues had begun, aimed at growing thin films of $LiAlO_2$, and was forced to stop after the

lab fire. With the lab recovering this work is set to begin again and will further push the boundaries of integrated nanostructure fabrication

2. The nucleation mechanism of RuO_2 may allow the fabrication of catalysts for a variety of applications including, microbial fuel cells and Li-air batteries. To this end new collaborations have been started with Professor Hu's group aimed at making RuO_2 catalyst nanoparticles on MWCNT sponges.
3. Finally in broader sense this work opens up the possibility of further integration of nanostructures into bulk energy storage cells. The problem of how to connect individual nanostructures to the bulk cell remains an active area of research and will require creative, simple, and cheap methods if these nanomaterials are going to be integrated into future commercially available devices.

6.3 Resulting Publications

1. **Gregorczyk**, **K**., Henn-Lecordier, K., Gatineau, J., Dussarrat, C., Rubloff, GW. Atomic Layer Deposition of Ruthenium Using the Novel Precursor bis(2,6,6-trimethyl-cyclohexadienyl)ruthenium. Chemistry of Materials. Vol. 23, Issue 10, 2650-2656. 2011.
   DOI: 10.1021/cm2004825

2. Banerjee, P., Chen, X., **Gregorczyk**, **K**., Henn-Lecordier, L., Rubloff, GW. Mixed mode, ionic-electronic diode using atomic layer deposition of V_2O_5 and ZnO films. Journal of Materials Chemistry. Vol. 21. Issue 29, 15391-15397. 2011.
   DOI: 10.1039/c1jm12595h

3. **Gregorczyk**, **K**., Banerjee, P., Rubloff, GW. Conduction in Ultrathin Ruthenium Electrodes Prepared by Atomic Layer Deposition. Materials Letters, 73, 43-46. 2012.
   DOI: 10.1016/j.matlet.2011.12.117

4. Chen, X., Pomerantseva, K., Banerjee, B., **Gregorczyk**, **K**., Ghodssi, R. and Rubloff, GW. Ozone-based Atomic Layer Deposition of Crystalline V_2O_5 Films for High Performance Electrochemical Energy Storage. Chemistry of Materials, 24 (7), 1255-1261. 2012.
   DOI: 10.1021/cm202901z

5. Chen, X., Pomerantseva, K., **Gregorczyk, K.**, Ghodssi, R. and Rubloff, G. Cathodic ALD V_2O_5 Thin Films for High-Rate Electrochemical Energy Storage. RSC Advances, *accepted*
   DOI: 10.1039/C3RA23031G

6. **Keith Gregorczyk**, Xinyi Chen, Marshall Schroeder, Alex Kozen, and Gary Rubloff. Atomic Layer Deposition of RuO_2: New Process Development and Fabrication of 3D MWCNT/RuO_2 Negative Battery Electrodes. *Manuscript in Preparation.*

7. **Keith Gregorczyk**, Yang Liu, John Sullivan, and Gary Rubloff. In-Situ TEM Study of Electrochemical Lithiation of the Conversion Anode RuO_2. *Manuscript in Preparation.*

Appendices

Appendix 1: A Table of Available Ru-Based ALD Precursors

Precursors	Growth Rate (A/Cycle)	Deposition Temperature (C)	Nucleation (# of cycles)	Substrates	Phase At RT	Precursor Temp	Reference
$RuCp_2$, Air	0.45	275-400	>100	Al_2O_3, TiO_2	Liquid	50	Aaltonen et al, Chem. Vap. Deposition 2003,9, No 1.
$Ru(Od)_3$, O_2	0.875	325-375	NR	CNT	Liquid	200	Min et al, Adv. Mater.2003,15 , No 12
$Ru(thd)_3$, O_2	0.36	325-450	>200	Al_2O_3	Solid	100	Aaltonen et al, Chem. Vap. Deposition, 2004, 10, No 4
$Ru(EtCp)_2$, O_2	1.5	270	NR	TiN	Liquid	80	Kwon et al, J. Electrochem. Soc, 151, 2004
$Ru(EtCp)_2$, NH_3 plasma	0.38	270	NR	TiN	Liquid	80	Kwon et al, J. Electrochemical and Solid-State Letters, 7, 2004.
Ru(DMPD)(EtCp), O_2	0.4	230-280	negligible	TiO_2, SiO_2, TiN	Liquid	200	Kim et al, J. Electrochem. Soc, 154, 2007
Ru(IPMB)(CHD), O_2	0.86	220	negligible	TiN, SiO_2	Solid	100	Eom et al, Electrochemical and Solid-State Letters, 12, 2009
$Ru(thd)_3$ (dissolved in ECH), O_2	NR	330-380	~75	Al_2O_3	Solid	NR	Kim et at, J. Phys. Chem. C 2009, 113, 11329-11335.
N,N-RuCp, Air	0.5	325-500	25-75	Al_2O_3	Solid	75-80	Kukli et al, J. Electrochem. Soc. 157, 2010
Ru(Cyprus), O_2	0.5	250-280	negligible, except Al_2O_3	Si, SiO_2, TiO_2, Al_2O_3	Liquid	60	This Work

Appendix 2: A Table of Available Ru-Based ALD Precursors That Mention RuO_2

Precursor	Publication(s)
bis(cyclopentadienyl)Ru, $RuCp_2$	Park, S.J., et al. Thin Solid Films, 2008. 516(21): p. 7345-7349.
bis(ethylcyclopentadienyl)Ru, $Ru(EtCp)_2$	Kwon, O.K., et al. Journal of the Electrochemical Society, 2004. 151(2): p. G109-G112 Kim, J.H., et al. Applied Physics Letters, 2007. 91(5) Kwon, S.H., et al. Journal of the Electrochemical Society, 2007. 154(9): p. H773-H777. Kim, W.H., et al. Journal of the Korean Physical Society, 2009. 55(1): p. 32-37 Salaun, A., et al. Chemical Vapor Deposition, 2011. 17(4-6): p. 114-122.
Bis(2,2,6,6-tetramethyl-3,5-heptanedionato)(1,5-cyclooctadiene)Ru, $Ru(thd)_2(COD)$	Husekova, K., et al. Thin Solid Films, 2010. 518(16): p. 4701-4704.
Cyclopentadienyl ethylruthenium dicarbonyl, $Ru(Cp)(CO)_2Et$	Park, S.K., et al. Chemistry of Materials, 2010. 22(17): p. 4867-4878.
bis(2,6,6-trimethyl-cyclohexadienyl)ruthenium, $Ru(C_9H_{13})_2$, ‘Cyprus’	Gregorczyk, et al. Chem. Mater. 2011. This work

References

1. Kirss, R.U., *Synthesis, characterization and spectroscopy of alkyl substituted edge-bridged open ruthenocenes.* Inorganica Chimica Acta, 2004. **357**(11): p. 3181-3186.
2. Law, M., J. Goldberger, and P.D. Yang, *Semiconductor nanowires and nanotubes.* Annual Review of Materials Research, 2004. **34**: p. 83-122.
3. Banerjee, P., et al., *Nanotubular metal-insulator-metal capacitor arrays for energy storage.* Nature Nanotechnology, 2009. **4**(5): p. 292-296.
4. Liu, R. and S.B. Lee, *MnO2/Poly(3,4-ethylenedioxythiophene) coaxial nanowires by one-step coelectrodeposition for electrochemical energy storage.* Journal of the American Chemical Society, 2008. **130**(10): p. 2942-2943.
5. Masuda, H., *Ordered Metal Nanohole Arrays Made by a Two-Step Replication of Honeycomb Structures of Anodic Alumina.* Science, 1995. **268**(5216): p. 1466-1468.
6. George, S.M., A.W. Ott, and J.W. Klaus, *Surface chemistry for atomic layer growth.* Journal of Physical Chemistry, 1996. **100**(31): p. 13121-13131.
7. Puurunen, R.L., *Surface chemistry of atomic layer deposition: A case study for the trimethylaluminum/water process.* Journal of Applied Physics, 2005. **97**(12).
8. Jung, Y.S., et al., *Enhanced Stability of LiCoO2 Cathodes in Lithium-Ion Batteries Using Surface Modification by Atomic Layer Deposition.* Journal of the Electrochemical Society, 2010. **157**(1): p. A75-A81.
9. Jung, Y.S., et al., *Ultrathin Direct Atomic Layer Deposition on Composite Electrodes for Highly Durable and Safe Li-Ion Batteries.* Advanced Materials, 2010. **22**(19): p. 2172-+.
10. Scott, I.D., et al., *Ultrathin Coatings on Nano-LiCoO2 for Li-Ion Vehicular Applications.* Nano Letters, 2011. **11**(2): p. 414-418.
11. Cheng, H.M., et al., *Enhanced Cycleabity in Lithium Ion Batteries: Resulting from Atomic Layer Depostion of Al2O3 or TiO2 on LiCoO2 Electrodes.* Journal of Physical Chemistry C, 2012. **116**(14): p. 7629-7637.
12. Lee, J.T., et al., *Low-temperature atomic layer deposited Al2O3 thin film on layer structure cathode for enhanced cycleability in lithium-ion batteries.* Electrochimica Acta, 2010. **55**(12): p. 4002-4006.
13. Jung, Y.S., et al., *Effects of Atomic Layer Deposition of Al2O3 on the Li[Li0.20Mn0.54Ni0.13Co0.13]O-2 Cathode for Lithium-Ion Batteries.* Journal of the Electrochemical Society, 2011. **158**(12): p. A1298-A1302.
14. Zhao, J.Q. and Y. Wang, *Ultrathin Surface Coatings for Improved Electrochemical Performance of Lithium Ion Battery Electrodes at Elevated Temperature.* Journal of Physical Chemistry C, 2012. **116**(22): p. 11867-11876.

15. Riley, L.A., et al., *Conformal Surface Coatings to Enable High Volume Expansion Li-Ion Anode Materials.* Chemphyschem, 2010. **11**(10): p. 2124-2130.
16. He, Y., et al., *Alumina-Coated Patterned Amorphous Silicon as the Anode for a Lithium-Ion Battery with High Coulombic Efficiency.* Advanced Materials, 2011. **23**(42): p. 4938-4941.
17. Riley, L.A., et al., *Improved Mechanical Integrity of ALD-Coated Composite Electrodes for Li-Ion Batteries.* Electrochemical and Solid State Letters, 2011. **14**(3): p. A29-A31.
18. Lahiri, I., et al., *Ultrathin alumina-coated carbon nanotubes as an anode for high capacity Li-ion batteries.* Journal of Materials Chemistry, 2011. **21**(35): p. 13621-13626.
19. Cheah, S.K., et al., *Self-Supported Three-Dimensional Nanoelectrodes for Microbattery Applications.* Nano Letters, 2009. **9**(9): p. 3230-3233.
20. Gerasopoulos, K., et al., *Self-assembled Ni/TiO2 nanocomposite anodes synthesized via electroless plating and atomic layer deposition on biological scaffolds.* Chemical Communications, 2010. **46**(39): p. 7349-7351.
21. Gerasopoulos, K., et al., *Biofabrication methods for the patterned assembly and synthesis of viral nanotemplates.* Nanotechnology, 2010. **21**(5).
22. Wang, W., et al., *Three-Dimensional Ni/TiO2 Nanowire Network for High Areal Capacity Lithium Ion Microbattery Applications.* Nano Letters, 2012. **12**(2): p. 655-660.
23. Donders, M.E., et al., *Co3O4 as anode material for thin film micro-batteries prepared by remote plasma atomic layer deposition.* Journal of Power Sources, 2012. **203**: p. 72-77.
24. Li, X.F., et al., *Tin Oxide with Controlled Morphology and Crystallinity by Atomic Layer Deposition onto Graphene Nanosheets for Enhanced Lithium Storage.* Advanced Functional Materials, 2012. **22**(8): p. 1647-1654.
25. Chen, X.Y., et al., *Ozone-Based Atomic Layer Deposition of Crystalline V2O5 Films for High Performance Electrochemical Energy Storage.* Chemistry of Materials, 2012. **24**(7): p. 1255-1261.
26. Gerasopoulos, K., et al., *Hierarchical Three-Dimensional Microbattery Electrodes Combining Bottom-Up Self-Assembly and Top-Down Micromachining.* ACS Nano, 2012. **6**(7): p. 6422-6432.
27. Pomerantseva, E., et al., *Electrochemical performance of the nanostructured biotemplated V2O5 cathode for lithium-ion batteries.* Journal of Power Sources, 2012. **206**: p. 282-287.
28. Chen, X., et al., *MWCNT/V2O5 Core/Shell Sponge for High Areal Capacity and Power Density Li-Ion Cathodes.* ACS Nano, 2012. **x**(x): p. x.
29. Bailar, J.C., et al., *Comprehensive Inorganic Chemistry*1973, Oxford: Pergamon.
30. Henrich, V.E. and A. Cox, *The Surface Science of Metal Oxides*1994, Cambridge.
31. Grillo, M.E., *Stability of corundum- versus rutile-type structures of ruthenium and rhodium oxides.* Physical Review B, 2004. **70**(18).

32. Ryden, W.D. and A.W. Lawson, *Electrical Transport Properties of Iro2 and Ruo2.* Physical Review B, 1970. **1**(4): p. 1494-&.

33. Haynes, W.M., ed. *CRC Handbook of Chemistry and Physics* 91 ed. 2010-2011.

34. Steeves, M.M., *Electronic Transport Properties of Ruthenium and Ruthenium Dioxide Thin Films*, in *Department of Physics*2011, The University of Maine: Orno

35. Zheng, J.P., P.J. Cygan, and T.R. Jow, *Hydrous Ruthenium Oxide as an Electrode Material for Electrochemical Capacitors.* Journal of the Electrochemical Society, 1995. **142**(8): p. 2699-2703.

36. Hu, C.C. and K.H. Chang, *Cyclic voltammetric deposition of hydrous ruthenium oxide for electrochemical capacitors: effects of codepositing iridium oxide.* Electrochimica Acta, 2000. **45**(17): p. 2685-2696.

37. Jeong, Y.U. and A. Manthiram, *Amorphous ruthenium-chromium oxides for electrochemical capacitors.* Electrochemical and Solid State Letters, 2000. **3**(5): p. 205-208.

38. Rolison, D.R., et al., *Multifunctional 3D nanoarchitectures for energy storage and conversion.* Chemical Society Reviews, 2009. **38**(1): p. 226-252.

39. Balaya, P., et al., *Fully reversible homogeneous and heterogeneous Li storage in RuO2 with high capacity.* Advanced Functional Materials, 2003. **13**(8): p. 621-625.

40. Delmer, O., et al., *Enhanced potential of amorphous electrode materials: Case study of RuO2.* Advanced Materials, 2008. **20**(3): p. 501-505.

41. Trasatti, S. and G. Buzzanca, *Ruthenium Dioxide - New Interesting Electrode Material - Solid State Structure and Electrochemical Behaviour.* Journal of Electroanalytical Chemistry, 1971. **29**(2): p. A1-&.

42. Hu, Y.S., et al., *Improved electrode performance of porous LiFePO4 using RuO2 as an oxidic nanoscale interconnect.* Advanced Materials, 2007. **19**(15): p. 1963-+.

43. Hu, Y.S., et al., *Electrochemical lithiation synthesis of nanoporous materials with superior catalytic and capacitive activity.* Nature Materials, 2006. **5**(9): p. 713-717.

44. Delmer, O. and J. Maier, *On the chemical potential of a component in a metastable phase-application to Li-storage in the RuO(2)-Li system.* Physical Chemistry Chemical Physics, 2009. **11**(30): p. 6424-6429.

45. George, S.M., *Atomic Layer Deposition: An Overview.* Chemical Reviews, 2010. **110**(1): p. 111-131.

46. Suntola, T. *Thirty Years of ALD. An Invited Talk at AVS Topical Conference on Atomic Layer Deposition.* in *ALD 2004*

. 2004. University of Helsinki: Helsinki, FInland.

47. Mikkulainen, V., et al., *Crystallinity of inorganic films grown by atomic layer deposition: Overview and general trends.* Journal of Applied Physics, 2013. **113**(021301).

48. Aaltonen, T., et al., *Ruthenium thin films grown by atomic layer deposition.* Chemical Vapor Deposition, 2003. **9**(1): p. 45-49.

49. Aaltonen, T., et al., *Reaction mechanism studies on atomic layer deposition of ruthenium and platinum.* Electrochemical and Solid State Letters, 2003. **6**(9): p. C130-C133.
50. Cordes, J.F. and S. Schreiner, *Dampfdruckmessungen Bei Einigen Aromatenkomplexen.* ZEITSCHRIFT FUR ANORGANISCHE UND ALLGEMEINE CHEMIE, 1959. **299**(1-2): p. 87-91.
51. Lei, W., Henn-Lecordier, L., Anderle, M., Rubloff, G.W., Barozzi, M., Bersani, M., *Real-time observation and optimization of tungsten atomic layer deposition process cycle.* Journal of Vacuum Science & Technology B, 2006. **24**(2): p. 780.
52. Henn-Lecordier, L., Lei, W., Anderle, M., and Rubloff, G.W., *Real-time sensing and metrology for atomic layer deposition processes and manufacturing.* Journal of Vacuum Science & Technology B, 2007. **25**(1): p. 130.
53. Necas, D. and P. Klapetek. http://www.gwyddion.net. 2010 [cited 2011].
54. Necas, D. and P. Klapetek. http://www.gwyddion.net. 2010 [cited 2012].
55. Green, M.L., et al., *Chemical Vapor-Deposition of Ruthenium and Ruthenium Dioxide Films.* Journal of the Electrochemical Society, 1985. **132**(11): p. 2677-2685.
56. Cho, S.K., et al., *Damascene Cu electrodeposition on metal organic chem-ical vapor deposition-grown Ru thin film barrier.* Journal of Vacuum Science & Technology B, 2004. **22**(6): p. 2649-2653.
57. Friedrich, K.A., et al., *CO adsorption and oxidation on a Pt(111) electrode modified by ruthenium deposition: An IR spectroscopic study.* Journal of Electroanalytical Chemistry, 1996. **402**(1-2): p. 123-128.
58. Chrzanowski, W. and A. Wieckowski, *Ultrathin films of ruthenium on low index platinum single crystal surfaces: An electrochemical study.* Langmuir, 1997. **13**(22): p. 5974-5978.
59. Lee, W.K., et al., *Distribution of Droplets on Ruthenium Thin Films Prepared by Pulse Nd:Yag Laser.* Informacije Midem-Journal of Microelectronics Electronic Components and Materials, 2010. **40**(2): p. 88-92.
60. Maiwa, H., N. Ichinose, and K. Okazaki, *Preparation and Properties of Ru and Ruo2 Thin-Film Electrodes for Ferroelectric Thin-Films.* Japanese Journal of Applied Physics Part 1-Regular Papers Short Notes & Review Papers, 1994. **33**(9B): p. 5223-5226.
61. Kwon, O.K., et al., *Atomic layer deposition of ruthenium thin films for copper glue layer.* Journal of the Electrochemical Society, 2004. **151**(2): p. G109-G112.
62. Shibutami, T., et al., *Ruthenium film with high nuclear density deposited by MOCVD using a novel liquid precursor.* Electrochemical and Solid State Letters, 2003. **6**(9): p. C117-C119.
63. Kim, S.K., et al., *Atomic layer deposition of Ru thin films using 2,4-(dimethylpentadienyl)(ethylcyclopentadienyl)Ru by a liquid injection system.* Journal of the Electrochemical Society, 2007. **154**(2): p. D95-D101.
64. Middleman, S. and A.K. Hochberg, *Process Engineering Analysis in Semiconductor Device Fabrication*1993, New York: McGraw-Hill.

65. Matero, R., et al., *Effect of water dose on the atomic layer deposition rate of oxide thin films.* Thin Solid Films, 2000. **368**(1): p. 1-7.
66. Kuse, R., et al., *Effect of precursor concentration in atomic layer deposition of Al2O3.* Journal of Applied Physics, 2003. **94**(10): p. 6411-6416.
67. Aaltonen, T., et al., *Atomic layer deposition of ruthenium thin films from Ru(thd)(3) and oxygen.* Chemical Vapor Deposition, 2004. **10**(4): p. 215-219.
68. Kwon, O.K., et al., *Plasma-enhanced atomic layer deposition of ruthenium thin films.* Electrochemical and Solid State Letters, 2004. **7**(4): p. C46-C48.
69. Kukli, K., et al., *High Temperature Atomic Layer Deposition of Ruthenium from N,N-Dimethyl-1-ruthenocenylethylamine.* Journal of the Electrochemical Society, 2010. **157**(1): p. D35-D40.
70. Gregorczyk, K., P. Banerjee, and G.W. Rubloff, *Conduction in ultrathin ruthenium electrodes prepared by atomic layer deposition.* Materials Letters, 2012. **73**: p. 43-46.
71. Kumar, A., G. Chandra, and O.P. Katyal, *The Study of Temperature-Coefficient of Resistivity of Polycrystalline Metal-Films.* Journal of Materials Science, 1988. **23**(7): p. 2361-2364.
72. Mayadas, A. And M. Shatzkes, *Electrical-Resistivity Model For Polycrystalline Films - Case Of Arbitrary Reflection At External Surfaces.* Phys Rev B, 1970. **1**(4): p. 1382-1389.
73. Mayadas, A.F., M. Shatzkes, and J.F. Janak, *Electrical Resistivity Model for Polycrystalline Films - Case of Specular Reflection at External Surfaces.* Applied Physics Letters, 1969. **14**(11): p. 345-&.
74. Zhang, Q.G., et al., *Influence of grain boundary scattering on the electrical and thermal conductivities of polycrystalline gold nanofilms.* Physical Review B, 2006. **74**(13): p. 134109-1 13109-5.
75. Puurunen, R.L. and W. Vandervorst, *Island growth as a growth mode in atomic layer deposition: A phenomenological model.* Journal of Applied Physics, 2004. **96**(12): p. 7686-7695.
76. Gregorczyk, K., et al., *Atomic Layer Deposition of Ruthenium Using the Novel Precursor bis(2,6,6-trimethyl-cyclohexadienyl)ruthenium.* Chemistry of Materials, 2011. **23**(10): p. 2650-2656.
77. Rubloff, G.W., et al., *Profile Evolution for Conformal Atomic Layer Deposition over Nanotopography.* Acs Nano, 2010. **4**(8): p. 4637-4644.
78. Li, H., et al., *Vapor deposition of ruthenium from an amidinate precursor.* Journal of the Electrochemical Society, 2007. **154**(12): p. D642-D647.
79. Vancea, J., G. Reiss, and H. Hoffmann, *Mean-Free-Path Concept in Polycrystalline Metals.* Physical Review B, 1987. **35**(12): p. 6435-6437.
80. Camacho, J.M. and A.I. Oliva, *Surface and grain boundary contributions in the electrical resistivity of metallic nanofilms.* Thin Solid Films, 2006. **515**(4): p. 1881-1885.
81. Eckertova, L., *Physics of Thin Films*. 2 ed1986, New York: Plenum Press.
82. Zabet-Khosousi, A. and A.A. Dhirani, *Charge transport in nanoparticle assemblies.* Chemical Reviews, 2008. **108**(10): p. 4072-4124.

83. Park, S.J., et al., *Effect oxygen exposure on the quality of atomic layer deposition of ruthenium from bis(cyclopentadienyl)ruthenium and oxygen.* Thin Solid Films, 2008. **516**(21): p. 7345-7349.
84. Kwon, S.H., et al., *Improvement of the morphological stability by stacking RuO2 on ru thin films with atomic layer deposition.* Journal of the Electrochemical Society, 2007. **154**(9): p. H773-H777.
85. Kim, W.H., et al., *Atomic Layer Deposition of Ruthenium and Ruthenium-oxide Thin Films by Using a Ru(EtCp)(2) Precursor and Oxygen Gas.* Journal of the Korean Physical Society, 2009. **55**(1): p. 32-37.
86. Salaun, A., et al., *Nucleation and Chemical Transformation of RuO2 Films Grown on (100) Si Substrates by Atomic Layer Deposition.* Chemical Vapor Deposition, 2011. **17**(4-6): p. 114-122.
87. Kim, J.H., et al., *Modified atomic layer deposition of RuO2 thin films for capacitor electrodes.* Applied Physics Letters, 2007. **91**(5).
88. Park, S.K., et al., *Atomic Layer Deposition of Ru/RuO2 Thin Films Studied by In situ Infrared Spectroscopy.* Chemistry of Materials, 2010. **22**(17): p. 4867-4878.
89. Husekova, K., et al., *Growth of RuO2 thin films by liquid injection atomic layer deposition.* Thin Solid Films, 2010. **518**(16): p. 4701-4704.
90. Min, Y.S., et al., *Ruthenium oxide nanotube arrays fabricated by atomic layer deposition using a carbon nanotube template.* Advanced Materials, 2003. **15**(12): p. 1019-+.
91. Mar, S.Y., et al., *Characterization of Ruo2 Thin-Films by Raman-Spectroscopy.* Applied Surface Science, 1995. **90**(4): p. 497-504.
92. Bottcher, A. and H. Niehus, *Formation of subsurface oxygen at Ru(0001).* Journal of Chemical Physics, 1999. **110**(6): p. 3186-3195.
93. Blume, R., et al., *Identification of subsurface oxygen species created during oxidation of Ru(0001).* Journal of Physical Chemistry B, 2005. **109**(29): p. 14052-14058.
94. Bottcher, A. and H. Niehus, *Oxygen adsorbed on oxidized Ru(0001).* Physical Review B, 1999. **60**(20): p. 14396-14404.
95. Madey, T.E., H.A. Engelhardt, and D. Menzel, *Adsorption of Oxygen and Oxidation of Co on Ruthenium (001) Surface.* Surface Science, 1975. **48**(2): p. 304-328.
96. Bates, J.B., et al., *Thin-film lithium and lithium-ion batteries.* Solid State Ionics, 2000. **135**(1-4): p. 33-45.
97. Jones, S.D., J.R. Akridge, and F.K. Shokoohi, *Thin-Film Rechargeable Li Batteries.* Solid State Ionics, 1994. **69**(3-4): p. 357-368.
98. Bates, J.B., et al., *Thin-Film Rechargeable Lithium Batteries.* Journal of Power Sources, 1995. **54**(1): p. 58-62.
99. Bates, J.B., et al., *Rechargeable Thin-Film Lithium Batteries.* Solid State Ionics, 1994. **70**: p. 619-628.
100. Dudney, N.J., *Solid-state thin-film rechargeable batteries.* Materials Science and Engineering B-Solid State Materials for Advanced Technology, 2005. **116**(3): p. 245-249.

101. Dudney, N.J. and B.J. Neudecker, *Solid state thin-film lithium battery systems.* Current Opinion in Solid State & Materials Science, 1999. **4**(5): p. 479-482.
102. Neudecker, B.J., N.J. Dudney, and J.B. Bates, *"Lithium-free" thin-film battery with in situ plated Li anode.* Journal of the Electrochemical Society, 2000. **147**(2): p. 517-523.
103. Cabana, J., et al., *Beyond Intercalation-Based Li-Ion Batteries: The State of the Art and Challenges of Electrode Materials Reacting Through Conversion Reactions.* Advanced Materials, 2010. **22**(35): p. E170-E192.
104. Balaya, P., et al., *Nano-ionics in the context of lithium batteries.* Journal of Power Sources, 2006. **159**(1): p. 171-178.
105. Zhukovskii, Y.F., et al., *Evidence for interfacial-storage anomaly in nanocomposites for lithium batteries from first-principles simulations.* Physical Review Letters, 2006. **96**(5).
106. Panda, S.K., et al., *Nanoscale size effect of titania (anatase) nanotubes with uniform wall thickness as high performance anode for lithium-ion secondary battery.* Journal of Power Sources, 2012. **204**: p. 162-167.
107. Rodrigues, S., N. Munichandraiah, and A.K. Shukla, *A review of state-of-charge indication of batteries by means of a.c. impedance measurements.* Journal of Power Sources, 2000. **87**(1-2): p. 12-20.
108. Arico, A.S., et al., *Nanostructured materials for advanced energy conversion and storage devices.* Nature Materials, 2005. **4**(5): p. 366-377.
109. Liu, X.H. and J.Y. Huang, *In situ TEM electrochemistry of anode materials in lithium ion batteries.* Energy & Environmental Science, 2011. **4**(10): p. 3844-3860.
110. Liu, X.H., et al., *In Situ TEM Experiments of Electrochemical Lithiation and Delithiation of Individual Nanostructures.* Advanced Energy Materials, 2012. **2**(7): p. 722-741.
111. Huang, J.Y., et al., *In Situ Observation of the Electrochemical Lithiation of a Single SnO2 Nanowire Electrode.* Science, 2010. **330**(6010): p. 1515-1520.
112. Zhong, L., et al., *Multiple-Stripe Lithiation Mechanism of Individual SnO2 Nanowires in a Flooding Geometry.* Physical Review Letters, 2011. **106**(24).
113. Zhang, L.Q., et al., *Direct observation of Sn crystal growth during the lithiation and delithiation processes of SnO2 nanowires.* Micron, 2012. **43**(11): p. 1127-1133.
114. Wang, C.M., et al., *In Situ Transmission Electron Microscopy Observation of Microstructure and Phase Evolution in a SnO2 Nanowire during Lithium Intercalation.* Nano Letters, 2011. **11**(5): p. 1874-1880.
115. Zhang, L.Q., et al., *Controlling the Lithiation-Induced Strain and Charging Rate in Nanowire Electrodes by Coating.* ACS Nano, 2011. **5**(6): p. 4800-4809.
116. Liu, X.H., et al., *In situ atomic-scale imaging of electrochemical lithiation in silicon.* Nature Nanotechnology, 2012. **7**(11): p. 749-756.
117. Liu, X.H., et al., *Size-Dependent Fracture of Silicon Nanoparticles During Lithiation.* ACS Nano, 2012. **6**(2): p. 1522-1531.
118. Liu, N., et al., *A Yolk-Shell Design for Stabilized and Scalable Li-Ion Battery Alloy Anodes.* Nano Letters, 2012. **12**(6): p. 3315-3321.

119. Karki, K., et al., *Lithium-Assisted Electrochemical Welding in Silicon Nanowire Battery Electrodes.* Nano Letters, 2012. **12**(3): p. 1392-1397.
120. McDowell, M.T., et al., *Studying the Kinetics of Crystalline Silicon Nanoparticle Lithiation with In Situ Transmission Electron Microscopy.* Advanced Materials, 2012. **24**(45): p. 6034-+.
121. Liu, X.H., et al., *Anisotropic Swelling and Fracture of Silicon Nanowires during Lithiation.* Nano Letters, 2011. **11**(8): p. 3312-3318.
122. Liu, X.H., et al., *Reversible Nanopore Formation in Ge Nanowires during Lithiation-Delithiation Cycling: An In Situ Transmission Electron Microscopy Study.* Nano Letters, 2011. **11**(9): p. 3991-3997.
123. Liu, X.H., et al., *In situ transmission electron microscopy of electrochemical lithiation, delithiation and deformation of individual graphene nanoribbons.* Carbon, 2012. **50**(10): p. 3836-3844.
124. Liu, Y., et al., *Lithiation-Induced Embrittlement of Multiwalled Carbon Nanotubes.* ACS Nano, 2011. **5**(9): p. 7245-7253.
125. Kushima, A., et al., *Leapfrog Cracking and Nanoamorphization of ZnO Nanowires during In Situ Electrochemical Lithiation.* Nano Letters, 2011. **11**(11): p. 4535-4541.
126. Liao, H.W., et al., *Interfacial Mechanics of Carbon Nanotube@ Amorphous-Si Coaxial Nanostructures.* Advanced Materials, 2011. **23**(37): p. 4318-4322.
127. Wang, J.W., et al., *Sandwich-Lithiation and Longitudinal Crack in Amorphous Silicon Coated on Carbon Nanofibers.* ACS Nano, 2012. **6**(10): p. 9158-9167.
128. Gu, M., et al., *In Situ TEM Study of Lithiation Behavior of Silicon Nanoparticles Attached to and Embedded in a Carbon Matrix.* ACS Nano, 2012. **6**(9): p. 8439-8447.
129. Ruzmetov, D., et al., *Electrolyte Stability Determines Scaling Limits for Solid-State 3D Li Ion Batteries.* Nano Letters, 2012. **12**(1): p. 505-511.
130. Wang, X., et al., *Revealing the conversion mechanism of CuO nanowires during lithiation-delithiation by in situ transmission electron microscopy.* Chemical Communications, 2012. **48**(40): p. 4812-4814.
131. Kim, M.H., et al., *Growth direction determination of a single RuO(2) nanowire by polarized Raman spectroscopy.* Applied Physics Letters, 2010. **96**(21).
132. Liu, Y.L., et al., *Growth of single-crystalline RuO2 nanowires with one- and two-nanocontact electrical characterizations.* Applied Physics Letters, 2007. **90**(1).
133. Neupane, S., et al., *Synthesis and characterization of ruthenium dioxide nanostructures.* Journal of Materials Science, 2011. **46**(14): p. 4803-4811.
134. Chen, C.C., et al., *The growth and characterization of well aligned RuO2 nanorods on sapphire substrates.* Journal of Physics-Condensed Matter, 2004. **16**(47): p. 8475-8484.
135. Liu, D.R. and D.B. Williams, *The Electron-Energy-Loss Spectrum of Lithium Metal.* Philosophical Magazine B-Physics of Condensed Matter Statistical Mechanics Electronic Optical and Magnetic Properties, 1986. **53**(6): p. L123-L128.

136. Mondio, G., F. Neri, and M. Allegrini, *Energy loss spectroscopy of RuO2 thin films.* Journal of Applied Physics, 1997. **82**(4): p. 1730-1735.
137. Zashkvar.Vv, V.S. Redkin, and Korsunsk.Mi, *Characteristic Electron Energy-Loss Spectrum for Ruthenium.* Soviet Physics Solid State,Ussr, 1970. **11**(8): p. 1944-&.
138. Chan, C.K., et al., *High-performance lithium battery anodes using silicon nanowires.* Nature Nanotechnology, 2008. **3**(1): p. 31-35.
139. Chan, C.K., X.F. Zhang, and Y. Cui, *High capacity Li ion battery anodes using Ge nanowires.* Nano Letters, 2008. **8**(1): p. 307-309.
140. Lee, W., et al., *Fast fabrication of long-range ordered porous alumina membranes by hard anodization.* Nature Materials, 2006. **5**(9): p. 741-747.
141. Masuda, H. and K. Fukuda, *Ordered Metal Nanohole Arrays Made by a 2-Step Replication of Honeycomb Structures of Anodic Alumina.* Science, 1995. **268**(5216): p. 1466-1468.
142. Nielsch, K., et al., *Self-ordering regimes of porous alumina: The 10% porosity rule.* Nano Letters, 2002. **2**(7): p. 677-680.
143. Lee, Y.J., et al., *Biologically Activated Noble Metal Alloys at the Nanoscale: For Lithium Ion Battery Anodes.* Nano Letters, 2010. **10**(7): p. 2433-2440.
144. Taillades, G. and J. Sarradin, *Silver: high performance anode for thin film lithium ion batteries.* Journal of Power Sources, 2004. **125**(2): p. 199-205.
145. Yu, Y., et al., *Reversible Storage of Lithium in Silver-Coated Three-Dimensional Macroporous Silicon.* Advanced Materials, 2010. **22**(20): p. 2247-+.
146. Gui, X.C., et al., *Soft, Highly Conductive Nanotube Sponges and Composites with Controlled Compressibility.* ACS Nano, 2010. **4**(4): p. 2320-2326.
147. Hu, L.B., et al., *Silicon-Carbon Nanotube Coaxial Sponge as Li-Ion Anodes with High Areal Capacity.* Advanced Energy Materials, 2011. **1**(4): p. 523-527.
148. Deng, S.L., et al., *Confined propagation of covalent chemical reactions on single-walled carbon nanotubes.* Nature Communications, 2011. **2**.
149. Meng, X.B., et al., *Heterostructural coaxial nanotubes of CNT@Fe2O3 via atomic layer deposition: effects of surface functionalization and nitrogen-doping.* Journal of Nanoparticle Research, 2011. **13**(3): p. 1207-1218.
150. Farmer, D.B. and R.G. Gordon, *Atomic layer deposition on suspended single-walled carbon nanotubes via gas-phase noncovalent functionalization.* Nano Letters, 2006. **6**(4): p. 699-703.